

R92-917992-3

AD-A254 543



(2)

# FATIGUE AND FRACTURE OF INTERMETALLIC ALLOYS

PREPARED BY

AFOSR-TR- 02 0798

C. V. Cooper  
H. R. P. Inoue  
A. F. Giamei  
L. H. Favrow

DTIC  
ELECTE  
AUG 21 1992  
S A D

FINAL REPORT

Contract F49620-89-C-0047

for

Air Force Office of Scientific Research  
Bolling Air Force Base  
Washington, DC 20332

✓  
\*Original contains color  
plates: All DTIC reproduct-  
ions will be in black and  
white\*

July 1992

92-23286



409 252

71p

92 8 20 071

Approved for public release;  
distribution unlimited.

# DISCLAIMER NOTICE



THIS DOCUMENT IS BEST QUALITY AVAILABLE. THE COPY FURNISHED TO DTIC CONTAINED A SIGNIFICANT NUMBER OF COLOR PAGES WHICH DO NOT REPRODUCE LEGIBLY ON BLACK AND WHITE MICROFICHE.

**REPORT DOCUMENTATION PAGE**Form Approved  
OMB No. 0704-0188

Public reporting burden for this collection of information is estimated to average 1 hour per response, including the time for reviewing instructions, searching existing data sources, gathering and maintaining the data needed, and reviewing the collection of information. Send comments regarding this burden estimate or any other aspect of this collection of information, including suggestions for reducing this burden, to Washington Headquarters Services, Directorate for Information Operations and Reports, 1215 Jefferson Davis Highway, Suite 1204, Arlington, VA 22202-4302, and to the Office of Management and Budget, Paperwork Reduction Project (0704-0188), Washington, DC 20503.

1. AGENCY USE ONLY (Leave blank)		2. REPORT DATE July 25, 1992		3. REPORT TYPE AND DATES COVERED Final, April 1, 1989 - March 31, 1992	
4. TITLE AND SUBTITLE Fatigue and Fracture of Intermetallic Alloys				5. FUNDING NUMBERS F49620-89-C-0047	
6. AUTHOR(S) C. V. Cooper, H. R. P. Inoue, A. F. Giamei, and L. H. Favrow					
7. PERFORMING ORGANIZATION NAME(S) AND ADDRESS(ES) United Technologies Corporation Research Center Silver Lane East Hartford, CT 06108 and University of Illinois at Urbana-Champaign, Urbana, IL 61801				8. PERFORMING ORGANIZATION REPORT NUMBER R92-917992-3	
9. SPONSORING/MONITORING AGENCY NAME(S) AND ADDRESS(ES) Air Force Office of Scientific Research Bolling Air Force Base Washington, DC 20332				10. SPONSORING/MONITORING AGENCY REPORT NUMBER	
11. SUPPLEMENTARY NOTES					
12a. DISTRIBUTION/AVAILABILITY STATEMENT Unlimited Approved for public release; distribution unlimited.				12b. DISTRIBUTION CODE	
13. ABSTRACT (Maximum 200 words) <p>The compound, <math>Al_3Ti</math>, was alloyed with 7.5 at.% Fe to produce a cubic <math>L_{12}</math> structure. This material was arc cast and either directly homogenization heat treated (HrHT) or comminuted into powder and consolidated by hot isostatic pressing (HIP). Microstructures were carefully evaluated by optical and electron microscopy. Mechanical properties were measured as a function of temperature using compression and flexure. Utilizing a novel test fixture, both monotonic and cyclic tensile properties were determined as a function of temperature for specimens which had been sequentially cast, HIPed, and HHTed. Despite quasi-brittle behavior below 1000°C, failure was within the gauge section in most cases. The fracture surfaces showed increasing evidence of ductile tearing as the temperature was increased, and pores were determined to play an important role in the fracture process. The yield strength vs. temperature response was relatively flat up to intermediate temperature, possibly attributable to competing slip systems. The compressive yield strength and strain to failure were typically greater than those measured in tension, particularly at the lower temperatures. The fatigue data were reasonably well behaved, with fatigue specimens showing clear evidence of striations. Attempts to alloy the binary <math>DO_{22}</math> compound with Nb did not produce the desired cubic structure.</p>					
14. SUBJECT TERMS Dislocations, ductile-to-brittle transition temperature, $L_{12}$ and $DO_{22}$ crystal structures, fatigue striations, electron microscopy.				15. NUMBER OF PAGES	
				16. PRICE CODE	
17. SECURITY CLASSIFICATION OF REPORT Unclassified	18. SECURITY CLASSIFICATION OF THIS PAGE Unclassified	19. SECURITY CLASSIFICATION OF ABSTRACT Unclassified	20. LIMITATION OF ABSTRACT None		

**Unclassified**

**SECURITY CLASSIFICATION OF THIS PAGE**

**CLASSIFIED BY:**

**N/A since Unclassified**

**DECLASSIFY ON:**

**N/A since Unclassified**

**SECURITY CLASSIFICATION OF THIS PAGE**

**Unclassified**



R92-917992-3

*Fatigue and Fracture of Intermetallic  
Alloys*

FINAL REPORT

Contract F49620-89-C-0047

Reported by

C. V. Cooper  
C. V. Cooper

Accession For	
NTIS CRA&I	<input checked="" type="checkbox"/>
DTIC TAB	<input type="checkbox"/>
Unannounced	<input type="checkbox"/>
Justification	
By	
Distribution	
Availability	
Dist	Availability for Special
A-1	

H. R. P. Inoue  
H. R. P. Inoue

A. F. Giamei  
A. F. Giamei

L. H. Favrow  
L. H. Favrow

DTIC QUALITY INSPECTED 8

Approved by

M. A. DeCrescente  
M. A. DeCrescente  
Manager of Mfg. Tech. and  
Process Research

DATE: July 1992

## CONTENTS

<u>Section</u>		<u>Page</u>
1.0	INTRODUCTION .....	1
1.1	Overview .....	1
1.2	Review of the Literature .....	2
1.2.1	Phase Equilibria and Microstructural Studies .....	2
1.2.2	Deformation Studies .....	3
2.0	EXPERIMENTAL PROCEDURES .....	5
2.1	Alloy Casting .....	5
2.2	Specimen Preparation and Heat Treatment .....	5
2.3	Microscopy .....	7
2.4	Mechanical Behavior .....	7
3.0	RESULTS AND DISCUSSION .....	8
3.1	Microstructures and Properties of Cast $\text{Al}_3\text{Ti} + \text{Fe}$ .....	8
3.1.1	Optical Microscopy in Undeformed Condition .....	8
3.1.2	TEM of As-Cast Material (Undeformed Condition) .....	8
3.1.3	TEM of Sequentially Cast and HHTed Material (Undeformed Condition) .....	8
3.1.4	Compressive Properties of Sequentially Cast and HHT Material .....	9
3.1.5	TEM of Sequentially Cast and HHT Material (Deformed in Compression to 0.5%) .....	10
3.1.6	Flexural Properties .....	10
3.2	Microstructures and Crystallographic Orientation of Second-Phase Precipitates .....	10

## **CONTENTS (CONT'D.)**

<b><u>Section</u></b>	<b><u>Page</u></b>
3.2.1 TEM Microstructures .....	10
3.2.2 Crystal Structure of Plate-Shaped Precipitates .....	11
3.3 Fracture Properties in HIPed and HHTed Conditions .....	12
3.3.1 Microstructures .....	12
3.3.2 Temperature Dependence of Yield Stress and Ductility .....	12
3.3.3 Fracture Morphologies .....	13
3.3.4 Dislocation Structure .....	14
3.4 The Effects of Iron Content .....	14
3.5 The Effects of Powder Size and Purity .....	15
3.6 Mechanical Properties of Sequentially Cast, HIPed, and HHTed Material .....	15
3.6.1 Compressive and Flexure Properties .....	15
3.6.2 Monotonic and Cyclic Tensile Properties .....	16
3.7 Niobium Alloy Studies .....	19
4.0 SUMMARY AND CONCLUSIONS .....	21
5.0 REFERENCES .....	23

## **FIGURES**

## 1.0 INTRODUCTION

### 1.1 OVERVIEW

Future generations of aircraft gas turbine engines will, most likely, utilize hot-section materials based on systems other than the now mature nickel-base superalloys. The identification of new systems has been motivated by the quest for higher combustion temperatures to satisfy the need for greater thrust-to-weight ratios and higher operating efficiencies. Among the potential systems is the broad class of materials known as intermetallics. Indeed, much research and development has gone into the study of intermetallic compounds based on the titanium-aluminum system, often with the focus on alloy development through ternary and quaternary additions as well as thermomechanical processing.

Three ordered compounds based on this binary system have been investigated to varying degrees:  $\text{Ti}_3\text{Al}$  ( $\alpha_2$ :alpha-2),  $\text{TiAl}$  ( $\gamma$ : gamma), and  $\text{Al}_2\text{Ti}$  ( $\eta$ : eta). Because of the increasing tendency to form oxidation-protective alumina films and its inherently low density ( $3.3 \text{ g/cm}^3$ ),  $\text{Al}_3\text{Ti}$  has held particular attraction. As with the  $\eta$  phase, a major difficulty with the  $\eta$  phase is inherent lack of ductility in the binary composition. Despite its intrinsic oxidation resistance,  $\text{Al}_3\text{Ti}$ , which in the binary form exhibits a  $\text{DO}_{22}$  (ordered tetragonal) crystal structure, has remained relatively understudied. The  $\text{DO}_{19}$  ( $\alpha_2$ ), the  $\text{L}_{10}$  ( $\gamma$ ), the  $\text{DO}_{22}$  ( $\eta$ ), and the well known  $\text{L}_{12}$  ( $\tau$ ) phases are all closed-packed and are related by variations in stacking and/or chemistry of the close-packed planes.

Through the addition of certain ternary transition metals, including iron, copper, or nickel, a phase transition from  $\eta$  to the ordered cubic,  $\text{L}_{12}$  can be induced. Being a crystal structure with higher symmetry over the  $\text{DO}_{22}$ , the  $\text{L}_{12}$  possesses potential advantages in mechanical behavior over the ordered tetragonal structure due to the increase in the number of active slip systems and the satisfaction of the well known Von Mises criterion for strain compatibility in polycrystals (Ref. 1).

Nonetheless, much research remains to be accomplished in the areas of understanding the exact mechanisms through which the  $\text{L}_{12}$  structure can be rendered increasingly ductile and the nature and location of the ductile-to-brittle transition phenomenon; furthermore, the entire areas of tensile and cyclic deformation remain virtually uninvestigated to date, at least in the open literature.

The attainment of the high symmetry,  $\text{L}_{12}$  structure is, of course, no guarantee that the alloy exhibits reasonable ductility. While the primary deformation mechanism in this structure, as discussed in greater detail below, is slip along octahedral planes, the cross slip of screw dislocations into cube planes creates sessile portions, which can lead to reduction in the tensile elongation to failure. High Peierls stresses may exist for certain dislocation dissociations, especially where fault energies are high (Refs. 2-8). Grain refinement, for example can lead to increases in flow stress, such that the cleavage stress is lower than the tensile yield stress. However, the cubic symmetry and close-packed nature of the  $\text{L}_{12}$  lattice offer the opportunity for useful ductility.



The intermetallic compounds of most interest show some solid solubility (i.e. they are not "line compounds") and are of high symmetry. The former condition preempts the possibility of forming small amounts of undesired equilibrium phases, while the latter condition maximizes the opportunities for multiple slip systems and the achievement of adequate low temperature fracture toughness. It turns out that the  $Al_3X$  compounds, where X is Ti or Nb, are  $DO_{22}$  compounds. This structure is closely related to  $L1_2$ , which is the crystal structure of the famous gamma prime phase. Even gamma prime has limited ductility under certain circumstances, but it is well understood and of great engineering significance. In addition, when  $Al_3Ti$  is alloyed with iron (or copper), the resultant  $L1_2$  structure has a finite phase field width.

## 1.2 REVIEW OF THE LITERATURE

**1.2.1 Phase Equilibria and Microstructural Studies**—Because of the extreme lack of tensile ductility and fracture toughness at room temperature for  $Al_3Ti$ , most recent studies, as noted above, have focused on alloying additions to induce the transformation from  $DO_{22}$  to  $L1_2$ . The first to report this phase transformation were Raman and Schubert (Ref. 9), who accomplished the transition by dilute alloying additions of copper, nickel, or zinc in substitution for aluminum. Similar phase transformation have been noted more recently by Seibold (Ref. 10) through substitutions of iron for aluminum. While required concentrations of the selected ternary additions vary, the typical range lies from five to fifteen atomic percent.

Many recent studies have concentrated on the specific effects of alloying additions and rapid solidification processing on the resulting microstructures and phase fields. For example, Huang, Hall and Giogliotti (Ref. 11) investigated rapidly solidified Al-Ni-Ti in the atomic ratio of 65Al:10Ni:25Ti and found predominantly but not exclusively cubic  $L1_2$  phase. Powers, Wert, and Turner (Ref. 12) considered nickel-modified  $Al_3Ti$ , prepared by the non-consumable arc melting technique, in the atomic ratio of 67Al:8Ni:25Ti. Non-single-phase structures consisting predominantly of  $L1_2$  were observed. Also, features exhibiting stacking-fault-like contrast were observed on  $\{001\}$  planes and were determined to be intrinsic stacking faults, which resulted from the dissociation of a  $\langle 110 \rangle \{001\}$  dislocations. These faults were determined to be sessile in nature and did not participate in the deformation process.

Tarnacki and Kim (Ref. 13) have examined arc-melted and rapidly solidified  $\tau$  phase which had been modified by copper additions leading to  $Al_5CuTi_2$ , or by small amounts of boron or manganese. Rapid solidification by melt-spinning was found to refine the microstructure significantly and increase the microhardness slightly compared to the as-cast alloy. The as-cast microstructure of the copper ternary was two-phase, with the primary phase described as having the "nominal composition" and the dispersed second phase being globules with sizes ranging from 3–20  $\mu m$ . X-ray diffraction analysis verified the  $L1_2$  crystal structure for both the as-cast and rapidly solidified forms. In addition, fine, second-phase particles on the order of 100 nm which were Cu-rich were resolved by TEM. While

mechanical property determinations were not the focus of Tarnacki and Kim's study, the addition of copper and the achievement of the  $L_{12}$  were observed to result in no improvements in ductility over the binary  $Al_3Ti$ .

Mazdiasni *et al.* (Ref. 14) examined the phase equilibria of iron, nickel, and copper-modified  $Al_3Ti$  prepared by vacuum arc melting. The resulting phase-field width was determined using x-ray diffraction of powder samples following homogenization and quenching from 800 and 1200°C. Single-phase  $\tau$  was found for all three ternary systems for the 1200°C isotherm. At 800°C, the width of the single-phase field was reduced for the iron and nickel ternary systems; the phase boundary was not determinable for the nickel ternary due to the nucleation of a fine, second-phase precipitate. These authors found that the  $L_{12}$  phase was stable to at least 1200°C in all three alloy systems.

However, Tarnacki and Kim (Ref. 15) failed to produce single-phase  $\tau$  in the Al-Ni-Ti ternary system despite a post-arc-melting homogenization heat treatment for 96 h at 1100°C in the  $Al_{67}Ni_8Ti_{25}$  ternary system.

A very exciting result from this laboratory (UTRC) is the achievement of phase-pure  $\tau$  in the iron ternary system. As is to be discussed further in section 3, single phase  $L_{12}$  with only isolated carbides, believed to be the result of impurities introduced with the iron, has been produced recently by the hot-pressing of prealloyed, comminuted powders. This has been achieved despite the well known difficulties associated with establishing equilibrium in peritectic systems.

To date, little information is available on the  $DO_{22}$  system,  $Al_3Nb$ . While the likelihood of transforming this system to phase-pure  $L_{12}$  remains unclear, unpublished reports indicate that additions of chromium, yttrium, and tungsten lead to a stable, oxidation-resistant, fracture-tough alloy. Furthermore, it should be possible to transform iron- and titanium-modified  $Al_3Nb$  to the  $L_{12}$  crystal structure through alloying, by analogy to  $Al_3Ti$ .

**1.2.2 Deformation Studies**—By comparison to the published literature dealing with microstructural and phase equilibria aspects, that which focuses on the deformation behavior of tau phase is rather scant. Recent studies of the deformation behavior of binary  $Al_3Ti$  ( $DO_{22}$ ) have been undertaken by Tamaguchi *et al.* (Refs. 16, 17). These authors have reported that the predominant deformation mode is that of deformation twinning on the (111) [112] system, which retains the  $DO_{22}$  lattice symmetry. At elevated temperatures, some evidence for deformation through slip in addition to twinning was noted by Burgers vector analysis; however, binary  $Al_3Ti$  has proven to be very brittle in tension at room temperature.

Deformation research in the iron-based  $L_{12}$  system has been conducted by Kumar and Pickens (Ref. 18) on ternary and quaternary-modified  $Al_{22}Fe_3Ti_8$ . Their study endeavored to promote a comparative understanding of the compressive behavior of  $\tau$  phase based on the ternary system and a 2 at.% vanadium (in substitution for titanium) quaternary alloy and to establish the temperature

dependence of the compressive flow stress. The major finding of their research was a substantial decrease in the magnitude of the positive dependence in the flow stress with temperature along with a second peak in the vanadium quaternary compared to the ternary alloy.

An investigation of the mechanical properties of a nickel-ternary  $\tau$  alloy, including compressive stress-strain and fracture toughness based on bend tests, was the focus of a recent paper by Turner, Powers, and Wert (Ref. 19). These authors reported substantial plasticity in compression ( $\epsilon_f \approx 14\%$ ) and a fracture toughness of  $3 \text{ MPa} \cdot \text{m}^{1/2}$ . Interestingly, the bend specimen fracture surfaces displayed major cleavage facet poles within a few degrees of [001], [110], [111], [112], and [113], which suggested that the alloy can fail on virtually any plane, the orientation of which is nearly perpendicular to the tensile axis. The lack of tensile ductility was explained by these researchers on the basis of the Rice-Thompson model (Ref. 20), in which dislocation emission from a crack tip inhibits or prevents plastic crack tip blunting as suggested by the  $Gb/\Gamma$  ratio being greater than 10, where  $G$  is the shear modulus,  $b$  is the Burgers vector, and  $\Gamma$  ("gamma") is the surface free energy.

Porosity and the presence of a more brittle second phase are additional problems which complicate the measurement of the tensile properties of the  $\tau$  phase. For example, Turner, Powers, and Wert (Ref. 19) report that, while the porosity of the as-cast alloys is quite low, the long-term, high-temperature homogenization heat treatment causes appreciable increases in porosity.

## 2.0 EXPERIMENTAL PROCEDURES

### 2.1 ALLOY CASTING

Intermetallic alloys for use in this program were prepared by arc melting using starting materials of two initial purities: (1) commercial purity and (2) high purity. In the latter of the two, close attention was paid to the elimination of impurities from the initial constituents which were believed to be deleterious to the cast ingots either during their cooling or during the subsequent determination of its properties. The chemical compositions of the starting constituents for the higher purity alloys are indicated in Table I. For both purities of starting materials, ingots were produced with a composition, in atomic percent, of 67.5% Al, 25% Ti, and 7.5% Fe. Arc casting was accomplished using a specially constructed, tri-electrode apparatus which was designed to accommodate batch-size maxima of between 150 and 250 g, depending on constituent and alloy density. Purified argon gas, gettered by flowing standard bottled gas over hot Ti chips, was used to create a protective atmosphere for the melting and solidification processes. As a measure to reduce nitrogen and oxygen impurity levels further, a titanium bar was melted in the chamber prior to melting the alloy constituents. Typical effluent impurity levels in the argon gas, monitored throughout the melting and casting procedures, were on the order of  $10^{-6}$  ppm by weight (one part impurity in  $10^{12}$  parts argon).

Buttons were cast in hemispherical, water-cooled copper hearths using a minimum of three melting and resolidification sequences; to minimize macrosegregation, the cast buttons were "flipped" between melting operations. In addition to the button configuration, drop castings of an iron alloy, by means of a small orifice in the copper hearth, were attempted as preliminary trials to the rapid solidification of the Fe-modified  $Al_3Ti$  alloy using a dual-wheel ribbon maker. This process was being assessed as an approach to the production of ultra-clean ribbon to be comminuted subsequently into powder. The arc-melting and rapid solidification apparatus were photographed and are presented in Figs. 1a-c.

To facilitate the production of the various specimen geometries, described below, ingots which were cast using the hemispherical hearth were secondarily cast in a flat-bottom hearth using procedures similar to those described above for the hemispherical hearth to produce plate castings.

### 2.2 SPECIMEN PREPARATION AND HEAT TREATMENT

Comminution of cast buttons from both the high purity and the nominal purity starting materials was accomplished using a standard ball mill with stainless steel comminutors, following which the alloy powders were graded with standard metal sieves. Ball milling and subsequent grading of powders were accomplished both in a protective atmosphere and in laboratory air, the former making use of an air-tight glove box following evacuation and a thorough purge with flowing argon. A schematic illustration of the glove box, in which comminution was accomplished in the presence of inert gas, is shown in Fig. 2. Powder which remained + 325 mesh following comminution, that is, that which failed

to pass through the 325 mesh sieve, was recycled through the ball milling and sieving processes. In order to determine the effects of powder size on the density and microstructure of hot pressings, powder which was sieved to -400 mesh was hot pressed and examined as well. These powders were hot pressed into plates using alumina inserts in titanium-zirconium-molybdenum (TZM) dies at a pressure of 34.5 MPa and a temperature of 1100°C for 4 h. Subsequent to their hot pressing, some plates were HIPed to increase density prior to fabrication into specimens.

Specimens of several geometries have been produced for study; both compression and flexure sample geometries have been produced from castings as well as compacted powders. The first of these is a thin beam, from which four-point flexure experiments have been conducted as a function of ambient temperature. The second of the specimen geometries is that of a right circular cylinder, from which monotonic, quasi-static compressive properties have been determined. For both geometries, high-purity buttons and plates were wire electro-discharge machined (EDM) in several heat-treated conditions. A determination of the mechanical properties of the lower purity castings was rendered impossible due to their spontaneous fracture following solidification during cooling to room temperature.

In addition to the as-cast (AC) condition, monotonic compression and flexure properties were determined from specimens in (1) a condition of hot isostatic pressing (HIP) followed by a homogenization heat treatment (HHT) and (2) the HHT condition, only. The homogenization heat treatment consisted of heating the machined specimens to 1100°C for 100 h in a controlled atmosphere furnace using argon gas which was purified in the same manner and to the same degree as described above for the casting process. Hot isostatic pressing (HIP), used to reduce the level of porosity compared to the as-cast condition, consisted of wrapping the ingots with Ta foil, placing the wrapped ingots in a stainless steel (SS) enclosure, evacuating, crimping, and sealing the SS container, placing the enclosed ingot in the pressure vessel, supplying an overpressure of argon to 8.3 MPa at approximately 25°C, elevating temperature to 1100°C and pressure to 172.4 MPa at approximately 25°C/min and 5.3 MPa/min, respectively, and holding at temperature and pressure for 4 h.

Tensile specimens were produced, as well, from processed (HIPed and HHTed, in sequence) castings and from powders (attritted castings); the castings were utilized for both monotonic and cyclic tensile experiments, whereas the powders were used for monotonic experiments, only. For the monotonic cyclic tensile experiments, a second HIP temperature of 1050°C was investigated in addition to the 1100°C HIP condition. The decision to limit the determination of cyclic tensile properties to include materials which were processed by sequentially HIPing and HHTing cast ingots was made for several reasons and included (1) an interest in reducing the enormous magnitude of the effort required to comminute the castings into powders of the size required for compaction to acceptable densities, (2) the low yield of powder of acceptable size range which resulted, irrespective of its time in the ball-milling apparatus, and (3) the hope that secondary-cast specimens could be treated in a much less labor-intensive fashion, such that the resulting specimens would possess a greater

percentage of theoretical density and consequent superior properties to those specimens which were processed from powders.

### **2.3 MICROSCOPY**

Optical (OM), scanning electron (SEM), and transmission electron microscopies (TEM) and selected area electron diffraction (SAED) have been applied in complementary fashion to characterize the microstructures of the Fe-modified  $\text{Al}_3\text{Ti}$  alloy in the AC and HHT conditions. To capitalize on mutual interests common to researchers at UTRC and the University of Illinois, UTRC has supplied undeformed and compressively deformed specimens to Professor H. R. P. Inoue of the Department of Materials Science and Engineering for TEM and electron diffraction analyses. Undeformed (virgin) and monotonically compressed cylindrical specimens were sectioned for TEM into discs having dimensions of 1 mm thickness and 4 mm diameter. The sectioning plane was perpendicular to the compressive axis, the axis of rotational symmetry for the cylinders, again accomplished using wire EDM. Discs for TEM were mechanically polished and subsequently electropolished to electron transparency using a twin-jet polisher. TEM and SAED were conducted using a Hitachi H-800 microscope operated at 200 keV.

### **2.4 MECHANICAL BEHAVIOR**

As noted above, the mechanical properties of AC, powder-processed, HHT, and HIP and HHT materials were determined by monotonic four-point flexure and compression experiments. Both configurations made use of a servo-hydraulic testing machine. The temperature range for testing was from 22 to 1100°C, and the strain rate was  $2.3 \times 10^{-5} \text{ s}^{-1}$ . All flexure and compression experiments were accomplished in an atmosphere of purified argon.

In addition, room- and elevated-temperature, monotonic and cyclic tensile experiments were performed on cast material which was HIPed and HHTed in sequence. The monotonic experiments were conducted as described above, and the cyclic experiments were carried out in load (stress) control using an R-ratio of 0.1 and a cyclic frequency of 20 Hz. For the latter, test temperatures of 22 and 1050°C were investigated, and stresses were applied which were equal to various fractions of the proportional yield stress at the test temperature to determine the resistance of the processed material to failure by fatigue. A second objective of the cyclic tensile experiments was to determine the tolerance of the material to inherent flaws (residual porosity and grain boundary defects) and its resistance to the initiation and subcritical propagation of microcracks from these residual pores.

### 3.0 RESULTS AND DISCUSSION

Unless otherwise specified, all reference to microstructures and properties within section 3 pertain to the alloy having the composition Al - 25 at.% Ti - 7.5 at.% Fe.

#### 3.1 MICROSTRUCTURES AND PROPERTIES OF CAST $\text{Al}_3\text{Ti} + \text{Fe}$

**3.1.1 Optical Microscopy in Undeformed Condition**—In contrast with reported x-ray diffraction results (Ref. 24), optical microscope observations showed that as-cast samples consist of a two-phase microstructure containing an  $\text{L}_{12}$  phase and a second phase, as shown in Fig. 3. This second phase has planar faults which may be twins which have formed in order to accommodate interfacial strain with the  $\text{L}_{12}$  matrix, as shown in Fig. 4. After homogenization, this second phase almost completely disappears; that is, the present alloy becomes essentially single phase with an  $\text{L}_{12}$  structure.

**3.1.2 TEM of As-Cast Material (Undeformed Condition)**—In the as-cast condition, a high density of dislocations with Burgers vectors of the type  $\langle 110 \rangle$  is observed. Some dislocations form dislocation networks and some are present individually. The dislocation network is composed of three types of  $\langle 110 \rangle$  dislocations. Characteristics of these microstructures are as follows: (1) dislocations are mostly curved or zigzagged; (2) dislocations show anomalous contrast, in that one side is sharp while the other side is not well defined, as shown in Fig. 5 (a, b, c, d); (3) dislocations show fine fringes (indicated by arrows), Fig. 5 (c); and (4) dislocation images are very wide, Fig. 5 (d), and show a lenticular structure, Fig. 5 (a). Close examination of these dislocations reveals that a second phase has precipitated in the form of thin plates along them. Such precipitates also occur on zigzagged portions of dislocations. In addition to these precipitates, the  $\text{L}_{12}$  matrix contains very thin plate-like precipitates which lie parallel to  $\{001\}$  planes and inside the grains. These appear near dislocations as lenticular precipitates. The size of these precipitates is 1 nm thick and 20–70 nm wide, as shown in Fig. 6. Extra diffraction spots from these fine precipitates do not appear in some  $\text{L}_{12}$  orientations, such as  $\langle 011 \rangle$ , but in other orientations, lattice tetragonality has been detected. The extra spots cannot be explained by assuming  $\text{DO}_{22}$  or  $\text{DO}_{23}$  structures. It has yet to be determined whether these fine precipitates possess the same crystal structure as that for precipitates which have formed along dislocations.

**3.1.3 TEM of Sequentially Cast and HHTed Material (Undeformed Condition)**—Quite different from the as-cast specimens, homogenized specimens exhibit essentially a single-phase  $\text{L}_{12}$  structure. The density of dislocations is much lower than that for the as-cast condition. No plate-like precipitates parallel to  $\{001\}$  planes have been observed. Close observation of the dislocations, however, reveals that there are some small precipitates which have nucleated on zigzagged dislocations, as shown in Fig. 7. These precipitates show fringe contrast similar to that for precipitates

observed in as-cast specimens. Hence, they are considered to possess the same crystal structure, although the size and shape are different. Because the volume fraction of this second phase is less than 1 percent, detection of its presence is impossible in standard x-ray diffraction experiments (Refs. 10, 24).

Selected area electron diffraction patterns taken parallel to various zone axes have revealed that this alloy consists primarily of an  $L_{12}$  phase for both as-cast and HHT conditions. Salient examples are shown in Fig. 8.

**3.1.4 Compressive Properties of Sequentially Cast and HHT Material**—Both as-cast and homogenized samples could be deformed to about 0.5% total strain without fracture at 22 and 1100°C in compression. It is noteworthy that, during preparation for electron microscopy, a homogenized sample was inadvertently compressed a few percent at room temperature without apparent fracture. However, all samples are quite brittle when deformed in tension.

Table II shows compressive test results obtained from both as-cast and homogenized samples. The compressive properties of the intermetallic alloy in AC and HHT conditions at test temperatures of 22 and 1100°C are presented graphically in Fig. 9. In all cases, the monotonic compression was terminated upon the achievement of approximately 0.5% strain, following which the cylindrical specimens were sectioned for TEM as described in section 2.3. None of the specimens fractured at either 22 or 1100°C upon the imposition of a compressive strain of this magnitude. For comparison, data for homogenized  $Al_{22}Ti_8Fe_3$  (i.e.  $Al_{66.7}Ti_{24.2}Fe_{9.1}$ ) samples (Ref. 18) are also shown in this table. As indicated, the room temperature yield stress of the present alloy, which contains 7.5 at.% Fe, is approximately 26% lower than that reported at 22°C for the alloy containing 9.2 at.% Fe. The slope of the dependence of the yield stress on temperature is less for the present alloy than for the alloy reported in Ref. 18, in that the extrapolated value for the latter at 1100°C is 30 MPa compared to the actual measured value for the current alloy of 98 MPa at 1100°C. It is suspected that the indigenous porosity present in the current alloy contributes to its comparative weakness.

While the 1100°C yield stress of this alloy is essentially the same for both the as-cast and homogenized samples, the room-temperature yield stress is 50% higher for as-cast samples. The presence of a second phase observed optically is not responsible for this difference in stress due to its large and blocky nature. As will be described below, transmission electron microscope observations of as-cast and homogenized samples have shown that this difference is caused by the presence of a high density of precipitates of a second phase(s). At 1100°C, dislocations probably moved without significant resistance from the observed precipitates due to a thermally activated process under applied stress; hence, both as-cast and homogenized specimens show almost equivalent yield stresses at elevated temperatures.



**3.1.5 TEM of Sequentially Cast and HHT Material (Deformed in Compression to 0.5%)**—Because small precipitates have nucleated on dislocations after homogenization, unpinning of the dislocations is expected to occur effectively when deformation occurs at room temperature, causing the upper- and lower-yield-point phenomenon which has been established to exist in plain carbon steels (Ref. 25). However, no such phenomenon has been observed. Differentiation of dislocations introduced during deformation from those present before deformation has been made possible by detecting the presence or absence of small precipitates on dislocations. Dislocations in specimens deformed at room temperature lie on  $\{111\}$  planes. On the other hand, most dislocations are curved in specimens deformed at  $1100^{\circ}\text{C}$ . Five out of the six possible  $\langle 110 \rangle$  type dislocations have been observed, as shown in Fig 10 and Table III. Stereoscopic observations reveal that some dislocations have cross slipped from  $\{111\}$  to  $\{001\}$  planes or vice versa. For example, dislocation 2, with a Burgers vector of  $[0\bar{1}1]$  in Fig. 10, lies on the  $(111)$  plane, and a screw portion of the dislocation has cross slipped onto the  $(100)$  plane. Similar cross slipping has been observed in other  $\text{L}_{12}$  compounds when deformed at high temperatures (Ref. 26).

**3.1.6 Flexural Properties**—The four-point flexural properties of the higher-purity alloy in the HHT conditions are summarized in Table IV, and the stress-strain responses are presented graphically in Fig. 11 for test temperatures of 22, 1200, and  $1300^{\circ}\text{C}$ . Viscous flow is exhibited throughout the stress-strain response, and no elastic modulus may be defined unambiguously. Conversely, the stress-strain response at  $22^{\circ}\text{C}$  is effectively purely elastic, and failure is in a brittle fashion. Without question, the measurement of the mechanical properties of the alloy is affected adversely by the significant volume fraction of porosity as documented in Figs. 3 and 4.

## **3.2 MICROSTRUCTURES AND CRYSTALLOGRAPHIC ORIENTATION OF SECOND-PHASE PRECIPITATES**

**3.2.1 TEM Microstructures** —As shown in Fig. 3, the second phase dispersions have planar faults, which possibly are twins. These faults might have formed in order to accommodate interfacial strain with the  $\text{L}_{12}$  matrix, as shown in Fig. 12. After homogenization, this second phase almost completely disappears; that is, the alloy becomes essentially single phase with an  $\text{L}_{12}$  structure. As shown in Fig. 13, TEM of sequentially cast and HHTed specimens reveals the presence of tiny precipitates on dislocation segments. Although it is not clear whether these tiny precipitates are the residues of the second phase which was present in abundance prior to HHT, they may play a significant role in providing good mechanical properties at high temperature. Since these precipitates are small in size and in quantity, characterization has been performed on the abundant, fine, plate-shaped precipitates from as-arc-cast specimens.

Two types of fine precipitates have been observed in as arc-cast specimens. Typical examples are shown in Figs. 14 and 6. Figure 14 shows fine band-shaped precipitates which have formed heterogeneously along grown-in and thermal-stress-induced dislocations, while Fig. 6 shows fine, plate-shaped precipitates which have formed homogeneously in grains of the  $\text{L}_{12}$  matrix. Such

heterogeneous precipitates are about 20 nm thick and show fringes with a fringe thickness of about 2–3 nm. These precipitates are considered to be similar to those observed in homogenized specimens, as shown in Fig. 6.

Microstructural observations have revealed that plate-shaped precipitates occur homogeneously parallel to {001} planes of L<sub>12</sub> matrix. In Fig. 6, plate-shaped precipitates clearly have formed parallel to (100) planes. The diffraction pattern taken from the area of this micrograph shows evident streaks, corresponding to precipitates parallel to {001} planes. Careful observation of this figure reveals that there are also precipitates which are parallel to (010) and (001) planes. The presence of precipitates which have formed on three sets of {001} planes is clearly evident in Fig. 15.

**3.2.2 Crystal Structure of Plate-Shaped Precipitates**—The crystal structure of plate-shaped precipitates which have formed on 001 planes was determined using electron diffraction patterns taken from arc-cast specimens. It was noticed that when the direction of the incident electron beam was parallel to zone axes of the matrix having low Miller indices, no extra diffraction spots were observed except streaks, which pass through diffraction spots of the L<sub>12</sub> matrix and are perpendicular to {001} planes of the matrix. They are, for example, [011], [111], and [121], as shown in Fig. 16(a,b,c). Conversely, many extra spots appeared in the case when the incident electron beam was parallel to zone axes having high Miller indices, as shown in Fig. 16(d,e,f). These extra spots cannot be indexed by assuming DO<sub>22</sub> and DO<sub>23</sub> structures, all of which are L<sub>12</sub>-based structures, as shown in Fig. 17(b,d). Taking into consideration that some extra spots appear at positions  $h/3$ ,  $k/3$ ,  $l/3$  and  $2h/3$ ,  $2k/3$ ,  $2l/3$ , where  $h$ ,  $k$ , and  $l$  are Miller indices of the L<sub>12</sub> matrix, another L<sub>12</sub>-based structure was assumed, which is composed of three L<sub>12</sub> unit cells, as shown in Fig. 17(c). However, this structure alone is unable to account for many of the extra spots observed.

A new ordered tetragonal structure proposed for the observed plate-shaped precipitates is shown in Fig. 18. The unit cell of this tetragonal structure is composed of six fcc unit cells containing 4 titanium atoms and 20 aluminum atoms. It should be noted that this structure is aluminum rich compared with the L<sub>12</sub>-based structures shown in Fig. 17. The atomic ratio (Al:Ti) of this proposed structure is 5:1, which is compared to a ratio of 3:1 for all the structures shown in Fig. 17. Although iron atoms are not shown in Fig. 18, they are considered to be located randomly at aluminum sites. Assuming this ordered tetragonal structure, all the diffraction patterns shown in Fig. 16 can be indexed.

In order to index the diffraction patterns shown in Fig. 16, the following lattice parameters are used:

$$\begin{aligned} a_{\text{ppt}} &= a_{\tau} = 0.394 \text{ nm, and} \\ c_{\text{ppt}} &= 6 \times a_{\tau} = 2.364 \text{ nm,} \end{aligned}$$

where  $\tau$  is the phase having L<sub>12</sub> crystal structure.

In addition, the following consideration is also needed. From the observations of the habit planes of the plate-shaped precipitates, there are six possible orientation relationships between this precipitate phase and the  $L_{12}$  matrix phase, suggesting the presence of six variants. However, due to equivalency, the total number of variants reduces to three. These three variants must be taken into account in indexing diffraction patterns taken from arc-cast specimens. The orientation relationships for these variants are as follows:

variant 1:    **a** [100] ppt // **a** [100]  $L_{12}$   
                  **b** [010] ppt // **b** [010]  $L_{12}$   
                  **c** [001] ppt // **c** [001]  $L_{12}$

variant 2:    **b** [010] ppt // **a** [100]  $L_{12}$   
                  **c** [001] ppt // **b** [010]  $L_{12}$   
                  **a** [100] ppt // **c** [001]  $L_{12}$

variant 3:    **c** [001] ppt // **a** [100]  $L_{12}$   
                  **a** [100] ppt // **b** [010]  $L_{12}$   
                  **b** [010] ppt // **c** [001]  $L_{12}$

Under the assumption of this proposed structure and these three orientation relationships, all extra spots can be indexed, as shown in Fig. 16(d,e,f).

### 3.3 FRACTURE PROPERTIES IN HIPED AND HHTED CONDITIONS

**3.3.1 Microstructures**—Previous optical microscope observations (Ref. 27) have revealed blocky second-phase precipitates in as-cast specimens. In addition, it has been observed by transmission electron microscopy that there are both fine platelets (10 nm wide), which have formed homogeneously along {001} planes, and band-shaped precipitates, which have formed heterogeneously along dislocations. After HIPing, such blocky precipitates disappear. In their place, structures with a dendritic morphology appear in the form of crosses, which seem to have a specific orientation relationship with the  $L_{12}$  matrix, as shown in Fig. 19. These could be "phantom" dendrites, a residual dendritic pattern which appears after precipitates nucleate and grow in the dendrite cores. After HHT annealing, conversely, the alloy becomes essentially single phase with a very small volume fraction of precipitates having nucleated along dislocations (Ref. 23). As will be shown below, room-temperature ductility is improved by HIPing. Hence, it is of great importance to identify microstructures of HIPed specimens and to determine the relationship between these microstructures and fracture properties.

**3.3.2 Temperature Dependence of Yield Stress and Ductility**—Both HHTed and HIPed specimens were deformed in compression at various temperatures. Yield stress values obtained were plotted as a function of test temperature. In contrast to the behavior commonly exhibited by ordered intermetallic alloys such as the nickel-based,  $L_{12}$  compounds of  $Ni_3Al$  and  $Ni_3Ge$ , the current alloy, which contains 7.5 at.% Fe, displayed no anomalous temperature dependence of the yield stress. As

shown in Fig. 20, the yield stress decreases slightly from room temperature to 400°C, remaining almost constant through 750°C, and then decreasing again at higher temperatures. Similar temperature dependence has been observed also in Pt<sub>3</sub>Al having the same L<sub>12</sub> structure (Ref. 29). The absence of an anomalous temperature dependence of yield stress in the present alloy is rather interesting because transmission electron microscope observations have revealed that screw dislocations cross slip from {111} to {001} planes in the alloy when deformed at 1100°C (Ref. 23). The relatively constant yield stress exhibited by the 7.5 at.% Fe alloy in the temperature range from 400 to 700°C may be considered to be a slight anomaly, for example compared to disordered fcc solid solutions, and is likely ascribable to dislocation cross-slip. Among many nickel-based L<sub>12</sub>-type compounds, such cross slipping is known to be the primary origin of the anomalous temperature dependence of the yield stress (Ref. 30).

Figure 20 also shows plastic strain obtained in the compression experiments. Compared with DO<sub>22</sub>-type Al<sub>3</sub>Ti, the modified L<sub>12</sub>-type Al<sub>3</sub>Ti alloy shows improvement in room-temperature ductility. Furthermore, as will be shown below in Fig. 21, room-temperature ductility is substantially improved after HIPing, although the *apparent* plastic strain (approximately 11%) obtained is almost the same for both HIPed and HHTed specimens. At temperatures higher than 400°C, both HHTed and HIPed specimens can be deformed to more than 12%. The proposed explanation for this behavior is that uniaxial compression tends to close existing pores and voids, reducing their contribution to the fracture event.

**3.3.3 Fracture Morphologies**—Figure 21 shows a portion of both HIPed and HHTed specimens deformed in compression at room temperature. Clearly evident is the brittle nature of the HHT condition. Specimens fracture into small pieces, and no original shape is retained, as shown in Fig. 21(a). Conversely, HIPed specimens retain their original shape even following the application of considerable plastic deformation (a strain of 11%). These specimens fracture by a few large vertical cracks propagating from top to bottom, as shown in Fig. 21(b).

High magnification scanning electron micrographs taken from the specimens in Fig. 21 reveal clear contrast of microstructural features. Figure 22(a) is a micrograph taken from region A of Fig. 21(a), where comparably large pieces are present, showing a high density of cavities. Fracture in this case occurs by brittle transgranular cleavage, which probably initiates at cavities formed upon solidification, Fig. 22(b). As is evident in this figure, fracture surfaces are relatively smooth but not parallel to any crystallographic planes with low Miller indices. Essentially similar structures are obtained from region B of Fig. 21(a), where the specimen in Fig. 21(a) becomes fragmented upon fracture. Compared to fracture surfaces for HHTed specimens, however, fracture surfaces are rather rough and irregular in the case of HIPed specimens, Fig. 22(c). In addition, both intergranular and transgranular fractures occur, as shown in Fig. 22(d). It should be noted that cavities are reduced significantly with retention of a small density of cavities after HIPing, as shown in Fig. 22(d). Intergranular fracture in this case has probably occurred due to strengthening against transgranular

fracture through the reduction in the size and density of cavities. Fracture surfaces of HIPed and HHTed specimens are also observed after deformation in compression at 400, 750, and 1100°C. In both cases, no significant change in fracture morphologies has been observed by increasing the test temperature, but it appears that fracture surfaces become more irregular and rugged with increasing temperature.

**3.3.4 Dislocation Structure**—The structure of dislocations introduced in HHT specimens by deformation in compression at room temperature has been investigated by means of HREM. Figure 23 is a micrograph taken from a thin foil parallel to the (001) plane, showing a pair of superlattice partial dislocations with a Burgers vector of  $a/2 [\bar{1}01]$  on a (111) plane. In the micrograph, the imaging atoms are considered to be titanium atoms located at the corner sites of the  $L1_2$  unit cells. Taking the lattice parameter of the alloy as 0.395 nm and the angle between the (001) and (111) planes into consideration, a spacing of 11 nm between the paired superlattice dislocations is obtained. It is obvious in this case that these dislocations do not lie on any {001} planes but lie on the (111) plane.

The APB energy,  $\gamma_{APB}$ , can be calculated using the equation for screw dislocations:

$$\gamma_{APB} = Gb^2/2\pi x,$$

where  $G$  is the shear modulus,  $b$  the Burgers vector, and  $x$  the spacing between two screw dislocations. Using a value for  $G$  of 84 GPa (Ref. 27), a Burgers vector for  $a/2[\bar{1}01]$  of 0.279 nm, and the measured superpartial separation of 11 nm, the APB energy is calculated to be 95 mJ/m<sup>2</sup>. This value is much lower than those reported for Al<sub>3</sub>Sc (313 mJ/m<sup>2</sup>) (Ref. 22) and Al-23Ti-6Fe-5V (274 mJ/m<sup>2</sup>) (Ref. 22). According to the Rice-Thomson criterion (Ref. 20), dislocations are considered to be emitted readily at or near crack tips for the present alloy due to the large separation between the two superpartial dislocations. However, the large separation between superpartial dislocations leads to greater difficulty in the ease with which dislocations may cross slip. This greater difficulty is likely to lead to reduced ductility and lower strain to failure, not the converse. Nonetheless, the Rice-Thompson criterion, applied alone, suggests that the alloy is intrinsically relatively ductile; hence, it should be possible to improve the ductility of this alloy through the complete elimination of porosity.

### 3.4 THE EFFECTS OF IRON CONTENT

To resolve the interesting microstructure noted in the cast and HIPed alloy containing 7.5 at.% Fe, Fig. 19, namely the presence of an interdendritic second phase pattern, master alloys containing 6.5 and 8.5 at.% Fe have been cast and resulting microstructures examined. While the alloy containing 8.5 at.% Fe failed to exhibit the interdendritic second phase, it continued to show the presence of a small volume fraction of second phase in the form of rods or islands in both the HIPed and HHTed

conditions. Interestingly, Morris (Ref. 29) reported single-phase microstructures for the ternary alloy in which 8.0 at.% Fe was added in substitution for Al. Conversely, the alloy which contained 6.5 at.% Fe was determined to have retained the interdendritic phase as well as the rod and island structure which was observed in the 8.5 at.% Fe alloy. By modifying the processing sequence such that HIPing preceded the HHT, nominally single-phase, L1<sub>2</sub> microstructures were obtained for the cast-HIPed-HHTed material containing 7.5 at.% Fe.

### **3.5 THE EFFECTS OF POWDER SIZE AND PURITY**

The microstructure and properties of hot pressed powder, which has been comminuted and graded to -325 or -400 mesh from the two purities of starting materials, have been determined. The major objective of this segment of the study has been to determine the influence of powder particle size on the microstructure and properties of the 7.5 at.% Fe alloyed with Al<sub>3</sub>Ti. Approximate measurements of specimens taken from hot-pressed plates demonstrated the existence of only insignificant differences in the densities of -325 and -400 mesh powders. Results obtained during this investigation have demonstrated that the the purity of starting materials had greater influence on tensile and flexure properties than did the original diameter of the hot-pressed powder. As noted above, the extreme labor intensity required to produce specimens through the powder route led to the decision to seek a less intensive processing route. However, a small number of tensile samples, strained to failure at 22°C, were processed via the powder route.

In order to study the tensile and fatigue properties at ambient and elevated temperatures, a fixture has been devised, as shown in Fig. 24. This fixture utilizes counter-rotating cams to grip "dogbone" shaped specimens, machined so as to closely approximate the cam profiles of the fixture. The cams rotate through radii of curvature profiles machined on specimen contact surfaces as well as the reverse side of the specimen contacting cams. This fixture allows for line loading of specimens in the radii and blend areas. In addition, as all four radii are loaded, this configuration produces specimen self-alignment. The fixture has been fabricated out of TZM for elevated temperature testing.

All specimens tested were comminuted to -400 mesh from the higher purity starting materials. In spite of the labor intensity which went into their production, rather disappointing quantities for the ultimate tensile strength, strain to failure, and elastic modulus were measured. Average measurements for these quantities were, respectively, 33.5 MPa, 0.12%, and 29 GPa. These disappointing properties led, in part, to the decision to seek an alternate processing route.

### **3.6 MECHANICAL PROPERTIES OF SEQUENTIALLY CAST, HIPED, AND HHTED MATERIAL**

In a fashion similar to that applied to determine the mechanical properties of cast, sequential cast and HIPed, and powder-processed Al<sub>3</sub>Ti, compressive, flexure, and monotonic and cyclic tensile properties of material in sequentially cast, HIPed, and HHTed condition have been determined.

**3.6.1 Compressive and Flexure Properties**—Compression of right cylindrical specimens at room temperature led to pseudoductility through shear crack formation and crumbling along grain boundaries and across grains. These factors, along with the constraint offered by the contact between the ends of the cylinder and the crosshead during compression, led to the observed compressive strains to failure of several percent. Monotonic compression experiments conducted as part of this program on sequentially cast, HIPed, and HHTed specimens produced apparent strains to failure of between 1.5 and 3.0 %, with significant scatter in the results, typifying the dependence of the measurement on the soundness of the material, most especially the size and volume fraction of pores. Modulus of elasticity measurements in compression, however, exhibited significantly less scatter and ranged from 195 to 216 GPa, which is not unexpected, in that the pores are placed in compression; strength measurements, similar to the trend exhibited by strain-to-failure data, ranged from 725 to 1050 MPa at 22°C. While ultimate compressive strengths showed marked sample-to-sample variation, both 0.2% offset and proportional limit stresses, the latter defined as the stress-strain response initially deviates from linearity, showed limited scatter. The former, for example, ranged from 204 to 216 MPa, while the latter ranged from 84.0 to 88.5 MPa.

Three-point flexure properties, in which the stress varies throughout the sample thickness and ranges from maximum tension to maximum compression, showed significantly lower strength and stiffness and failed in the linear elastic portion of the stress-strain diagram, which is indicative of entirely brittle failure. Elastic moduli ranged from 65 to 81 GPa, and bend strengths ranged from 106 to 172 MPa.

### **3.6.2 Monotonic and Cyclic Tensile Properties**

**3.6.2.1 Specialized Fixture**—As noted earlier, a special fixture, designed and constructed from TZM, allowed for the determination of true tensile properties of the alloy at ambient and elevated temperatures. The fixture, described in section 3.5, utilized rotating cams to grip the inside shoulders of EDMed tensile specimens in a self-aligning fashion. Representative specimens which have been EDMed from sequentially cast, HIPed, and HHTed Al - 25 at.% Ti - 7.5 at. % Fe are presented in Fig. 25a-c in the as EDMed, mechanically polished through 600 grit SiC, and mechanically polished and strain-gauged conditions, respectively. True tensile properties were determined at 22, 800, and 1050°C for materials which had been HIPed at one of two temperatures, either 1050 or 1100°C, followed by the standard HHT anneal before properties determinations. A constant crosshead speed of approximately  $2 \mu\text{m s}^{-1}$  was used for a gauge length of approximately 25 mm. For elevated-temperature experiments, special quartz extensometer rods were fabricated to eliminate uncertainties in the reporting of failure strain quantities.

**3.6.2.2 Monotonic Tension**—The two HIP temperatures resulted in appreciably variant microstructures in terms of residual porosity. Optical micrographs showing representative microstructures of the two HIP conditions are shown in Figs. 26 and 27 for the 1050 and 1100°C HIP,

respectively. Automated quantitative metallography showed porosity values to be within approximately 35% for the two HIP temperatures, being an average of 1.04 and 0.77 vol.% for the 1050 and 1100°C HIP temperatures, respectively; the difference in terms of pore size if not volume fraction, however, is significant for the two HIP temperatures.

Significant differences in the monotonic tensile properties between the two HIP temperatures was noted, and the salient data are summarized in Table V. Limited quantities of specimens precluded careful statistical analysis; however, the table indicates clearly that the sample which had been HIPed at 1100°C and tested at 1050°C showed significant ductility, while the sample which was HIPed and subsequently tested at 1050°C showed essentially no plastic strain at failure.

It is important to note that the ductile-to-brittle transition apparently lies at a temperature which is between 800 and 1050°C for the material which was sequentially cast, HIPed, and HHTed. Evidence to support this suggestion comes from the observation that the specimens which were HIPed at 1100°C exhibit real plastic strain prior to failure when tested at 1050°C. Conversely, the specimens which were HIPed *and* tested at 1050°C fail to exhibit significant plastic strain during monotonic tensile failure. However, a clear dependence of other properties, such as strength and elastic modulus, on the HIP temperature fails to emerge. While the average size of the pores decreases with increasing HIP temperature, the tensile properties are controlled by the size of the largest flaw, not that of the average flaw.

Examination of Figs. 28 and 29, SEM micrographs of the monotonic fracture surfaces of specimens which had been HIPed at 1050 and 1100°C, respectively, show that porosity played an important role in the fracture process, although the failure initiation sites are unclear. Clearly, the extent and size of porosity is much greater, at least as it participated in the fracture event, for the lower temperature HIP. Examination of Fig. 28b, a fracture surface following monotonic tension at 1050°C, reveals that the size of the pores seems to have grown, despite the quite limited time at test temperature. In addition, gross examination of the fracture surfaces shows that the fracture at 1050°C leads to the presence of dimples, characteristic of a more ductile failure. With the exception of their outer edges, the surfaces of the specimens which were tested at 22°C, conversely, exhibit essentially cleaved surfaces.

**3.6.2.3 Cyclic Tension**—In a similar manner, the cyclic tensile data exhibited significant scatter, which seemed to depend in a loose manner on the HIP temperature. As noted above for the monotonic tension experiments, a critical shortage of samples precluded careful and thorough statistical analysis of failure in cyclic tension, and many samples were claimed in handling mishaps or during the development of the required experimental procedures.

For this reason, cyclic tensile experiments were initiated at a maximum stress level which equalled 60% of the material's proportional yield stress, as determined in the monotonic tension experiments at temperatures of 22, 800, and 1050°C. The achievement of  $10^6$  cycles without failure at a



given stress amplitude allowed for an increase, typically of 10% of the monotonic proportional yield stress, in the applied maximum cyclic stress until failure was achieved within  $10^6$  cycles. As noted above, an R-ratio of 0.1 has been employed for all cyclic tensile experiments. Due to specimen shortage, the cyclic experiments were restricted to the two test temperatures of 22 and 1050°C, one above and one below the ductile-to-brittle transition temperature.

For the material which was HIPed at 1100°C and tested at 22°C, the number of cycles to failure at constant cyclic stress amplitude was relatively repeatable. Of three successful experiments of this type, all survived a stress level of 18.5 MPa; however, while two survived the required number of cycles at a maximum cyclic stress of 21.5 MPa, the third survived only 18,800 cycles at this stress. When the maximum cyclic stress level was increased to 24.5 MPa, only one of the three specimens endured any cycles at this level; it failed after only 4 cycles. Only one specimen which had been HIPed at the lower temperature of 1050°C was tested at 22°C; it failed following fewer than 10 cycles at a maximum stress level of 18.5 MPa.

At the test temperature of 1050°C, two samples which had been HIPed at 1100°C were cycled in tension at a maximum stress level of 21.7 MPa. Of the two, one survived 452,000 cycles, or approximately half of the goal of  $10^6$  cycles; the second specimen, however, failed on loading to the target stress level, failing at a stress of approximately 19.5 MPa. For the specimens which had been HIPed at a temperature of 1050°C and tested at 1050°C in cyclic tension, performance was found to be inferior to that of specimens which were HIPed at 1100°C and tested at 1050°C. With a goal for the maximum stress of 28.3 MPa, one specimen failed on monotonic loading at a stress of 24.0 MPa. A second specimen was cycled successfully at the lower maximum stress level of 21.7 MPa, failing after 42,600 cycles. The cyclic stress-life data for both HIP temperatures and both test temperatures are summarized graphically in Fig. 30.

It is clear from these data that, while the lower HIP temperature leads to significantly larger residual pores and higher volume fraction of porosity, the effect on the performance in cyclic tension is not entirely clear; it appears, based on the limited data generated for this program, that the specimens which had been HIPed at the higher temperature were able to endure higher cyclic stress levels than the specimens which had been HIPed at the lower temperature. This trend seems to hold for both test temperatures investigated.

SEM examination of fracture surfaces was successful, occasionally, in revealing the failure initiation sites; for cases in which SEM failed to reveal failure initiation sites, it remains extremely likely that residual porosity played a key role.

As shown in Fig. 31, a fracture surface from a specimen which had been HIPed at 1050°C and cycled at 22°C, the initiation sites often involved pores which were near or connected to the free surface. It appears from this figure that a very small amount of subcritical crack propagation preceded the final catastrophic event, as evidenced by the fatigue striations which emanate from the initiation

site. It is likely that this specimen, which endured  $10^6$  cycles at 21.5 MPa and failed following 4 cycles at 24.4 MPa, experienced subcritical crack growth during the cyclic stressing at 21.5 MPa.

The presence of fatigue striations as a demonstration of subcritical crack propagation is strikingly evident in Fig. 32, a SEM fractograph of a specimen which had been HIPed at 1100°C and failed at 22°C following 18,800 cycles at a maximum stress of 21.5 MPa. As in Fig. 31, the failure initiation site appears to have been a rather large defect which lay near or possibly connected to the free surface of the specimen.

Another SEM fractograph which demonstrates the tendency for the material to exhibit subcritical crack growth during cyclic tension at 1050°C is shown in Fig. 33. Taken following the HIP treatment at 1100°C and following 452,000 cycles at a maximum stress of 21.7 MPa, this figure shows a clear failure initiation site and fatigue striations emanating from the initiation site. In this case, however, the initiation site is clearly not connected to the surface but lies somewhat subsurface. The fracture area which is at the surface shows the classic dimple features, characteristic of ductile, elevated temperature fracture.

### 3.7 NIOBIUM ALLOY STUDIES

In an attempt to determine their potential as high-temperature materials, a series of Nb-containing alloys was prepared using the same casting techniques presented in section 2.2. For all alloys in this series, Nb was added in substitution for Ti, and the Al and Fe contents remained constant at 67.5 and 7.5 at.%, respectively. Following tri-electrode arc casting, these quaternary compositions were pulverized using a standard mortar and pestle and homogenization heat treated for 240 h (10 days) at 1100°C. The additional time at temperature, which exceeded that adopted for the standard HHT, was employed to ensure that the resulting microstructures had achieved their equilibrium phase(s). On these HHT treated powders, x-ray diffraction spectra were determined using a standard diffractometer using Cu K $\alpha$ .

Three compositions were investigated as follows (in atomic per-cent): (1) Al - 16.75 Ti - 8.25 Nb - 7.5 Fe, designated BE91-06, (2) Al - 8.25 Ti - 16.75 Nb - 7.5 Fe, designated BE91-07, and (3) Al - 25 Nb - 7.5 Fe, designated BE91-05. In this manner, the atomic percentage of Nb was increased linearly until, for BE91-05, Nb was added to the exclusion of Ti, resulting in a Al<sub>3</sub>Nb plus Fe alloy. The results of the phase analysis, as determined using x-ray diffraction, were not as promising as had been expected; in contrast to the Al-Ti-Fe ternary system, none resulted in essentially phase-pure L<sub>12</sub>. For example, the -06 composition, micrographs of which are presented in Fig. 34, exhibited approximately equal percentages of DO<sub>22</sub> and L<sub>12</sub> with a small percentage of a third, unidentified phase. Similarly, both -07 and -05, representative microstructures of which are presented in Figs. 35 and 36, respectively, showed the complete absence of the L<sub>12</sub> phase, with microstructures being predominated by the DO<sub>22</sub> phase and a small volume fraction of the same unidentified phase. The absence of phase-pure L<sub>12</sub> in the

series of niobium alloys is in contrast to modeling predictions for ternary  $\text{Al}_3\text{Nb}$  with Ni additions (Ref. 31). These calculations, which are based on electronic total energies, predict that, for Ni concentrations greater than 12.5 atomic percent, phase-pure  $\text{L1}_2$  should result, a prediction which has been confirmed experimentally by certain researchers (Ref. 32) and refuted by others (Ref. 33). Because of the disappointing crystallographic results, no fabrication of test specimens was attempted for the Nb-alloy series which contained iron.

#### 4.0 SUMMARY AND CONCLUSIONS

The crystal structure of the stoichiometric  $\text{Al}_3\text{Ti}$  intermetallic compound can be modified from the  $\text{DO}_{22}$  to the  $\text{L}_{12}$  structure by adding 7.5 at.% Fe to substitute for a portion of aluminum. This alloy is essentially single phase after homogenization at  $1100^\circ\text{C}$  for 100 h with a very small volume fraction of precipitates having formed along dislocations. Conversely, in the case of the as-cast condition, the alloy contains band-like precipitates which have formed along dislocations and a high density of very thin, plate-shaped precipitates which are parallel to  $\{001\}$  planes of the  $\text{L}_{12}$  matrix. The crystal structure of these plate-shaped precipitates is proposed to be an ordered tetragonal structure consisting of six fcc unit cells stacked along the "c" axis. This proposed structure contains 4 titanium atoms and 20 aluminum atoms with iron atoms in substitution for aluminum atoms. All diffraction patterns obtained were indexed by assuming this structure and two or three variants of the precipitate phase. Since there is a possibility that titanium atoms can be located at positions other than those proposed, detailed intensity calculations of diffraction patterns or high resolution electron microscopy may be needed to determine atom positions accurately.

In addition, the room temperature ductility of an  $\text{L}_{12}$ -type  $\text{Al}_3\text{Ti}$  alloy containing 7.5 at.% Fe has shown little improvement following hot isostatic pressing (HIP) after arc casting. However, fracture occurs at room temperature by brittle transgranular cleavage with a smooth surface in HHTed specimens, while in HIPed specimens, fracture occurs by both transgranular and intergranular modes. Transgranularly fractured surfaces in the latter case have rough surfaces with fine structure, indicating ductile fracture, in contrast to the behavior and fracture morphology of HHTed specimens. In both HIPed and HHTed specimens, no fracture surfaces are flat and parallel to any crystallographic planes. High resolution electron microscopy has revealed that a pair of superlattice partial dislocations on a (111) plane have a spacing of approximately 11 nm (2–3 times larger than that for  $\text{Al-23Ti-6Fe-5V}$ ), indicating an antiphase boundary energy of  $95 \text{ mJ/m}^2$ . Since this energy is relatively low, the present alloy may be ductile because of its ready emission of dislocations at crack tips, according to the Rice-Thomson criterion. Improvement in the room-temperature ductility of this alloy is attributed primarily to the reduction of a large population of cavities which have formed upon arc casting.

Monotonic tensile experiments which were conducted on sequentially cast, HIPed, and HHTed material indicated that the ductile-to-brittle transition temperature lies between  $800$  and  $1050^\circ\text{C}$ . However, the extreme flaw intolerance of the material manifests itself, in that specimens which were HIPed at  $1100^\circ\text{C}$  and contained smaller volume fraction and size of pores continued to exhibit limited tensile plastic strains to failure. Because of the larger size and higher density of pores in specimens which were given the  $1050^\circ\text{C}$  HIP, they failed in a brittle fashion and exhibited no plastic strain during testing at  $1050^\circ\text{C}$ . While the porosity was more deleterious to the material which had been HIPed at  $1050^\circ\text{C}$ , pores clearly played a major role relating to specimen fracture in monotonic tension for both HIP conditions. Cyclic tensile experiments showed less pronounced differences in properties between

the two HIP conditions; some cyclic tensile conditions seemed to be somewhat reproducible, uncharacteristic of failure in a material which is highly flawed. Fatigue striations were noted commonly for both HIP conditions and both test temperatures, which constituted evidence of subcritical crack growth from the preexistent flaws. Subcritical crack growth was observed to be more significant and extensive in specimens which had been cycled in tension at elevated temperature.

An investigation into quaternary Nb additions failed to produce the desired phase-pure  $L_{12}$  structure. Due to this situation, the mechanical properties of the Nb series of alloys were not investigated.

## 5.0 REFERENCES

1. R. Von Mises, *Z. Ang. Math. Mech.*, 8, 161 (1928).
2. S. M. Copley, B. H. Kear, and G. M. Rowe, *Mater. Sci. Eng.*, 10, 87 (1972).
3. B. H. Kear, A. F. Giamei, J. M. Silcock, and R. K. Ham, *Scripta Metall.*, 2, 287 (1968).
4. B. H. Kear, A. F. Giamei, G. R. Leverant, and J. M. Oblak, *Scripta Metall.*, 3, 455 (1969).
5. B. H. Kear, J. M. Oblak, and A. F. Giamei, *Proc. Second Int'l Conf. on Strength of Metals and Alloys*, 1155 (1970).
6. B. H. Kear, J. M. Oblak, and A. F. Giamei, *Metall. Trans.*, 1, 2477 (1970).
7. B. H. Kear, A. F. Giamei, and J. M. Oblak, *Scripta Metall.*, 4, 567 (1970).
8. J. E. Doherty, A. F. Giamei, and B. H. Kear, *Metall. Trans. A*, 6A, 2195 (1975).
9. A. Raman and K. Schubert, *Z. Metallkd.*, 56, 99 (1965).
10. A. Seibold, *Z. Metallkd.*, 72, 712 (1981).
11. S. C. Huang, E. L. Hall, and M. F. X. Gigliotti, *J. Mater. Res.*, 3, 1 (1988).
12. W. O. Powers, J. A. Wert, and C. D. Turner, *Philos. Mag. A*, 60, 227 (1989).
13. J. Tarnacki and Y. W. Kim, *Scripta Metall.*, 22, 329 (1988).
14. S. Mazdiasni, D. B. Miracle, D. M. Dimiduk, M. G. Mendiratta, and P. R. Subramanian, *Scripta Metall.*, 23, 327 (1989).
15. J. Tarnacki and Y.-W. Kim, in *Dispersion Strengthened Aluminum Alloys*, Editors Y.-W. Kim and W. M. Griffith, Warrendale, PA: The Metallurgical Society, 741 (1988).
16. M. Yamaguchi, Y. Umakoshi, and T. Yamane, *Philos. Mag. A*, 55, 301 (1987).
17. M. Yamaguchi, Y. Umakoshi, and T. Yamane, in *High Temperature Ordered Intermetallic Alloys II*, Editors N. S. Stoloff, C. C. Koch, C. T. Liu, and O. Izumi, Pittsburgh: Materials Research Society, 207 (1987).
18. K. S. Kumar and J. R. Pickens, *Scripta Metall.*, 22, 1015 (1988).
19. C. D. Turner, W. O. Powers, and J. A. Wert, *Acta Metall.*, 37, 2635 (1989).
20. J. R. Rice and R. Thompson, *Philos. Mag.*, 29, 73 (1974).

21. S. Zhang, J. P. Nic, and D. E. Mikkola, *Scripta Metall.*, 24, 57 (1990).
22. E. P. George, W. D. Porter, H. M. Henson, W. C. Oliver, and B. F. Oliver, *J. Mater. Res.*, 4, 78 (1989).
23. H.-R. Pak, C. M. Wayman, L. H. Favrow, C. V. Cooper, and J. S. L. Pak, in *Alloy Phase Stability and Design*, Editors G. M. Stocks, D. P. Pope, and A. F. Giamei, Pittsburgh: Materials Research Society, 357 (1991).
24. W. D. Porter, K. Hisatsune, C. J. Sparks, W. C. Oliver, and A. Dhere, *Mat. Res. Soc. Symp. Proc.* 133, 657 (1989).
25. A. H. Cottrell, *Dislocations and Plastic Flow in Crystals*, London: Oxford University Press, 140 (1953).
26. H.-R. Pak, T. Saburi, S. Nenno, and T. Ujiro, *Scripta Metall.*, 13, 1171 (1979).
27. E. P. George, J. A. Horton, W. D. Porter, and J. H. Schneibel, *J. Mater. Res.*, 5, 1639 (1990).
28. D. G. Morris, *J. Mater. Res.*, 7, 868 (1992).
29. D. M. Wee, O. Noguchi, Y. Oya, and T. Suzuki, *Trans. Jpn. Inst. Met.*, 21, 237 (1980).
30. H.-R. Pak, T. Saburi, and S. Nenno, *Trans. Jpn. Inst. Met.*, 18, 617 (1977).
31. H. R. P. Inoue, M. Kitamura, C. M. Wayman, and H. Chen, *Philos. Mag. Lett.*, 63, 345 (1991).
32. K. Schubert, H.-G. Meissner, A. Raman, and W. Rossteutscher, *Naturwissenschaften*, 51, 287 (1964).
33. P. R. Subramanian, J. P. Simmons, M. G. Mendritta, and D. M. Dimiduk, *Mater. Res. Symp. Proc.*, 133, 51 (1989).

**TABLE I**  
**ANALYZED IMPURITY LEVELS IN PPM OF HIGH-PURITY**  
**STARTING MATERIALS**

Impurity	Constituent		
	Ti	Al	Fe
Al	0.2		<1
Ag			<1
B	0.007		
Ca	0.1		<1
Cl	1		
Co	0.3		20
Cr	5	0.43	2
Cu	3	0.91	3
Fe	25	0.71	
K	0.8		
Li	0.1		
Mg	0.2	0.67	
Mn	1	0.21	
Na	0.3		
Nb	0.04		
Ni	3		3
P	0.002		
Si	0.6	4	60
Sn			10
Th		2	
Ti		0.81	
U		2	
V	0.5	0.18	
W	1		
Zn		0.46	
Zr	0.8	0.56	
H	18		
N	10		
C	100		
O	335		



**TABLE II**  
**COMPRESSIVE YIELD STRESS (0.2% OFFSET) FOR**  
 **$\text{Al}_{66.7}\text{Ti}_{24.2}\text{Fe}_{9.1}$**

Specimen	Test Temperature (°C)	Yield Stress (MPa)
$\text{Al}_{67.5}\text{Ti}_{25}\text{Fe}_{7.5}$ AC	22	280
	1100	102
$\text{Al}_{67.5}\text{Ti}_{25}\text{Fe}_{7.5}$ HHT	22	192
	1100	98
$\text{Al}_{66.7}\text{Ti}_{24.2}\text{Fe}_{9.1}$ HHT	22	370
	400	460
	750	250
	1100	30 (extrapolated)
(Ref. 18)		

**TABLE III**  
**BURGERS VECTORS OF DISLOCATIONS (FIG. 10) IN AN HHT SPECIMEN**  
**DEFORMED 0.5% AT 1100°C. THE  $g \cdot b = 0$  CRITERION WAS USED. "o" and "x"**  
**STAND FOR OUT OF AND IN CONTRAST, RESPECTIVELY**

<b>g\b</b>	<b>110</b>	<b>110</b>	<b>101</b>	<b>101</b>	<b>011</b>	<b>011</b>
<b>111</b>	<b>x</b>	<b>o</b>	<b>o</b>	<b>x</b>	<b>o</b>	<b>x</b>
<b>200</b>	<b>x</b>	<b>x</b>	<b>x</b>	<b>x</b>	<b>o</b>	<b>o</b>
<b>020</b>	<b>x</b>	<b>x</b>	<b>o</b>	<b>o</b>	<b>x</b>	<b>x</b>
<b>dislocation</b>	<b>1,6</b>	<b>7</b>	<b>-</b>	<b>4</b>	<b>3</b>	<b>2,5</b>

**TABLE IV**  
**FOUR-POINT FLEXURE PROPERTIES FOR  $\text{Al}_{67.5}\text{Ti}_{25}\text{Fe}_{7.5}$**   
**CASTINGS IN HHTed CONDITION**

Test Temperature (°C)	$\sigma_{\text{max}}$ (MPa)	$\sigma_{\text{PL}}$ (MPa)	E (GPa)	$\epsilon_e$ , $\epsilon_p$ , $\epsilon_T$ (%)
22	148.1	N/A	168.8	0.086 (all elastic)
1200	18.7	12.6	82.0	0.019, 0.898, 0.917
1300	1.5	N/A	N/A	0.512 (plastic)

$\sigma_{\text{max}}$  = stress at extreme outer fiber corresponding to maximum load

$\sigma_{\text{PL}}$  = stress at proportional limit in extreme outer fiber

E = Young's modulus in flexure

$\epsilon_e$  = elastic strain at fracture

$\epsilon_p$  = plastic strain at fracture

$\epsilon_T$  =  $\epsilon_e + \epsilon_p$

**TABLE V**  
**TENSILE DATA FROM CAST + HIP + HHT SPECIMENS**  
**COMPOSITION: Al<sub>67.5</sub>Ti<sub>25</sub>Fe<sub>7.5</sub>**

HIP Temp. (°C)	YS (MPa)	<b>Sigma</b> UTS (MPa)	E (GPa)	$\epsilon_f$ (%)	Test Temp. (°C)
1050	9.6	17.9	88.2	0.236	22
1050	N/A	28.9	28.2	0.103	1050
1050	N/A	43.4	N/A	N/A	1050
1100	8.9	21.8	62.7	0.287	22
1100	-	59.4	22.6	0.240	800
1100	-	46.7	N/A	N/A	800
1100	-	42.6	17.5	0.242	1025
1100	22.4	33.7	N/A	3.700	1050

- = elastic

N/A = not available

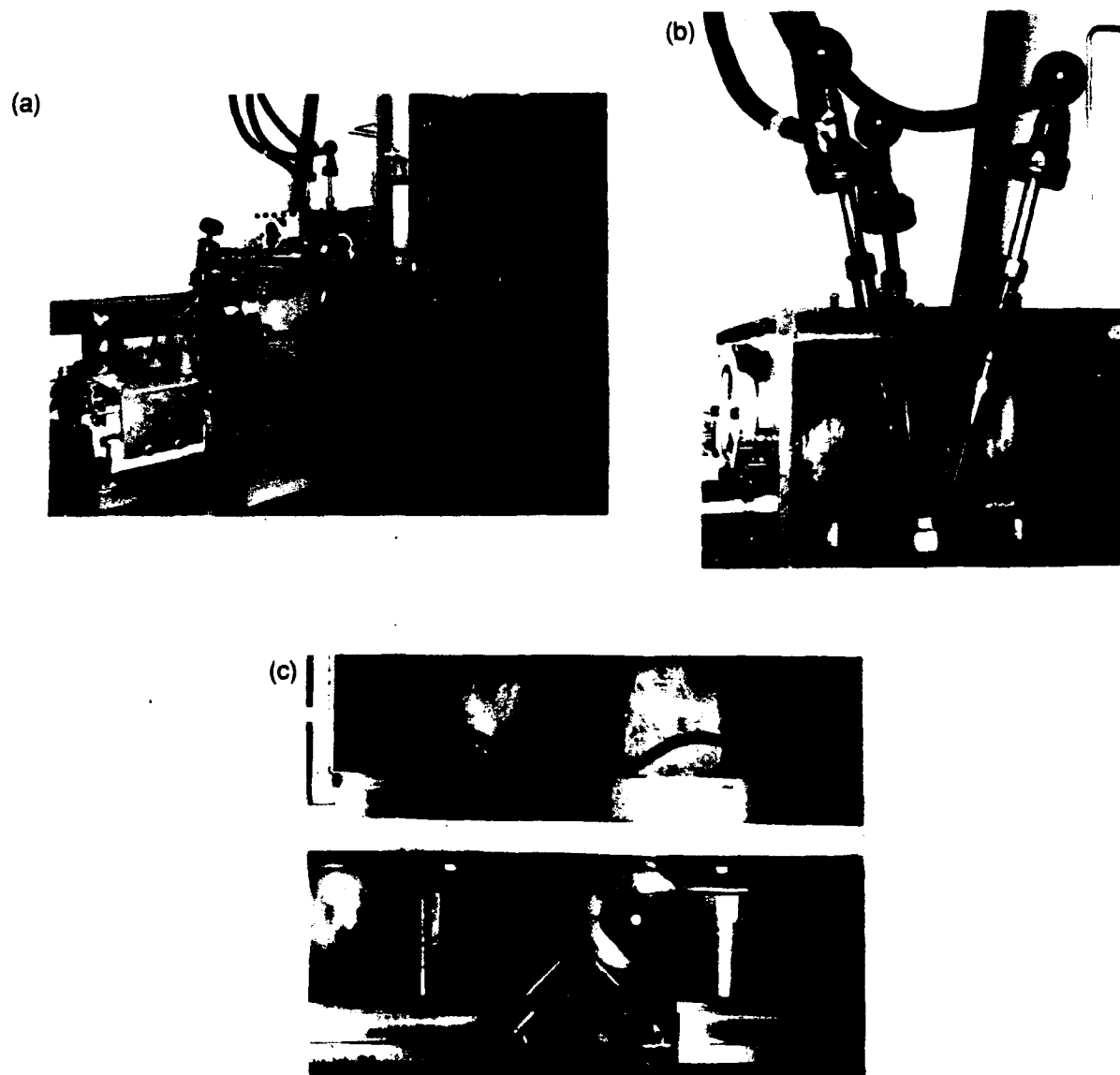


**Figure 1. UTRC Tri Arc Melter/Drop Caster Dual Wheel (RSR) Ribbon Maker. (a) External overview of unit, (b) Tri arc melting and casting section, and (c) Dual wheel ribbon making section.**

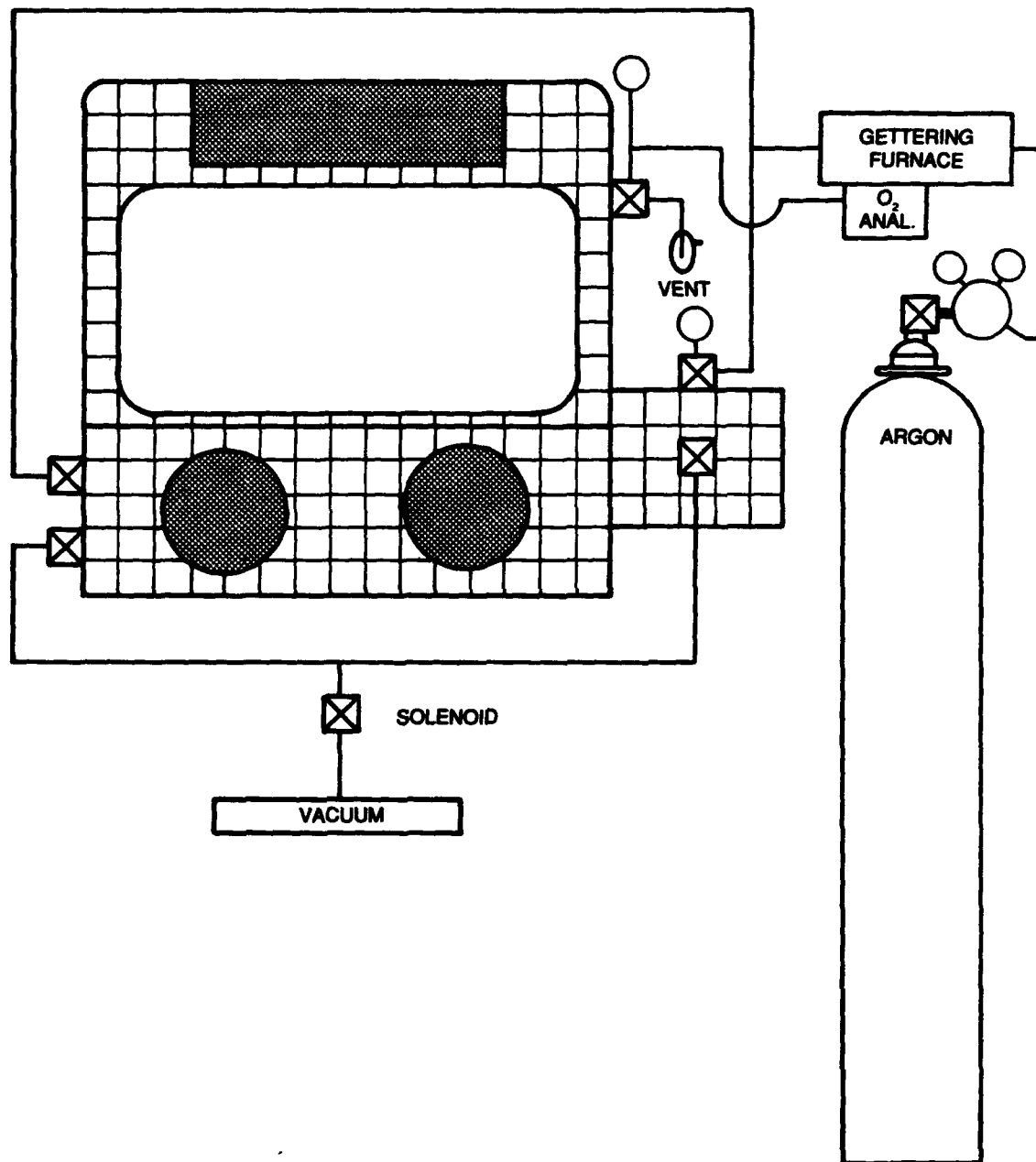


**Fig. 2 Schematic illustration of UTRC inert-environment glove box used for producing and handling elemental and alloy powders.**

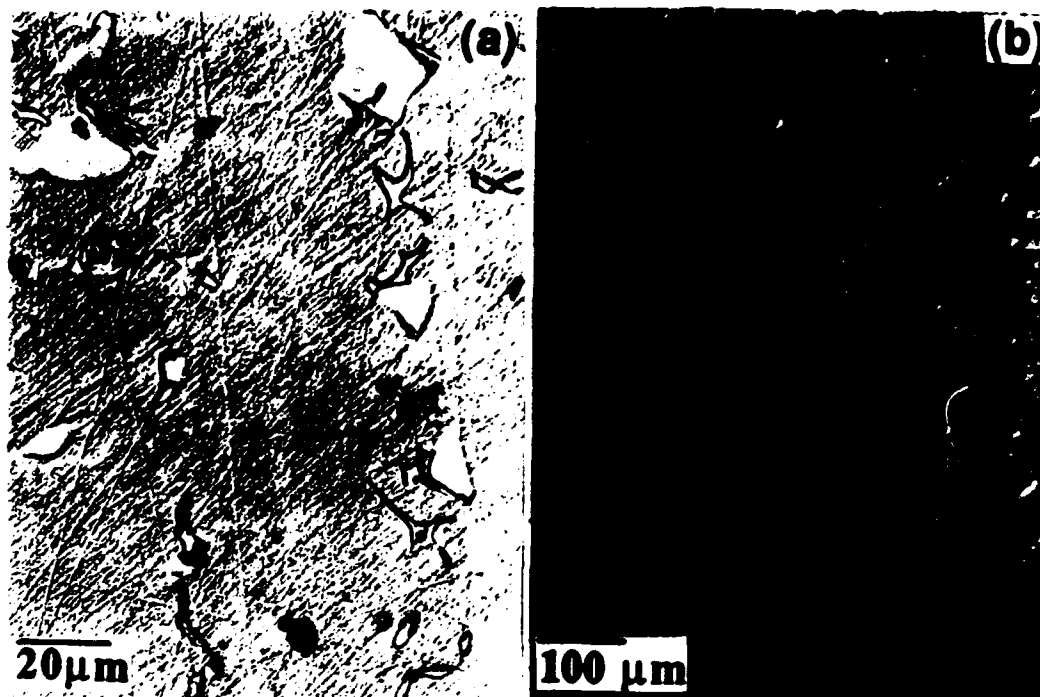


Figure 3. Optical micrographs of Fe-modified  $\text{Al}_3\text{Ti}$  in (a) as-cast (AC) and (b) homogenization-heat-treated (HHT) conditions.



**Figure 4. Scanning electron micrographs demonstrating indigenous porosity of Fe-modified  $\text{Al}_3\text{Ti}$  in (a) AC and (b) HHT conditions.**



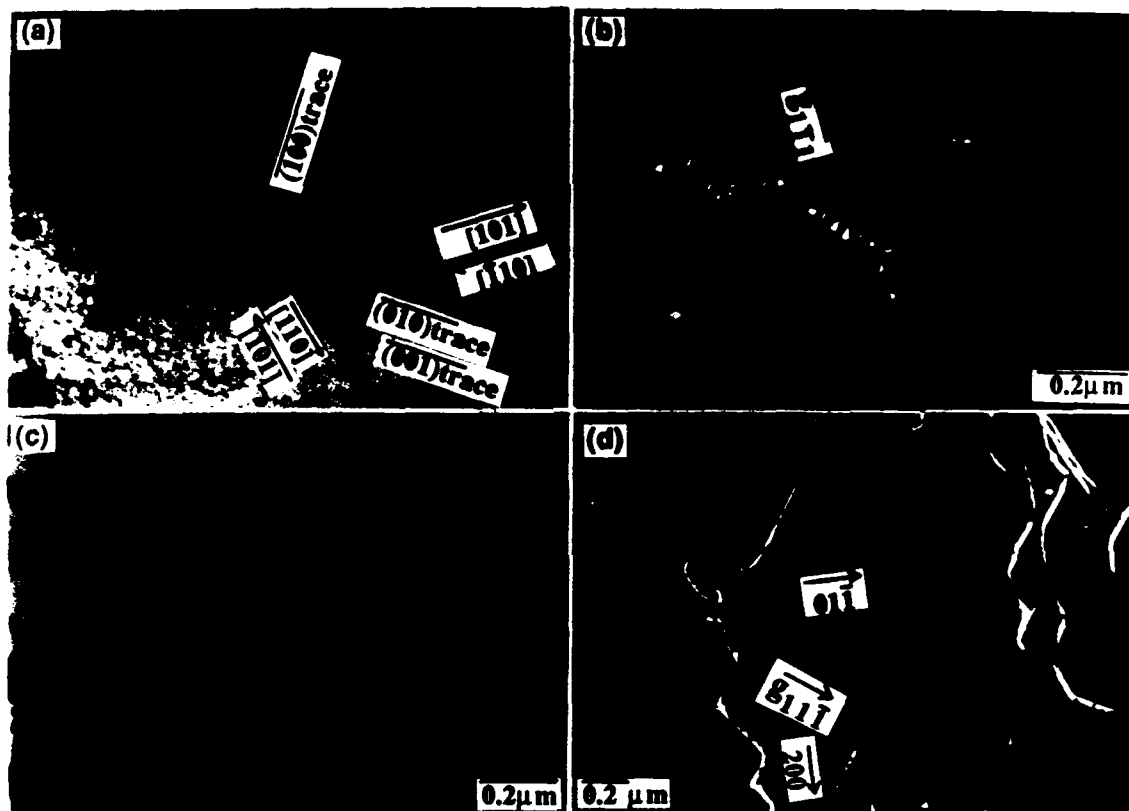
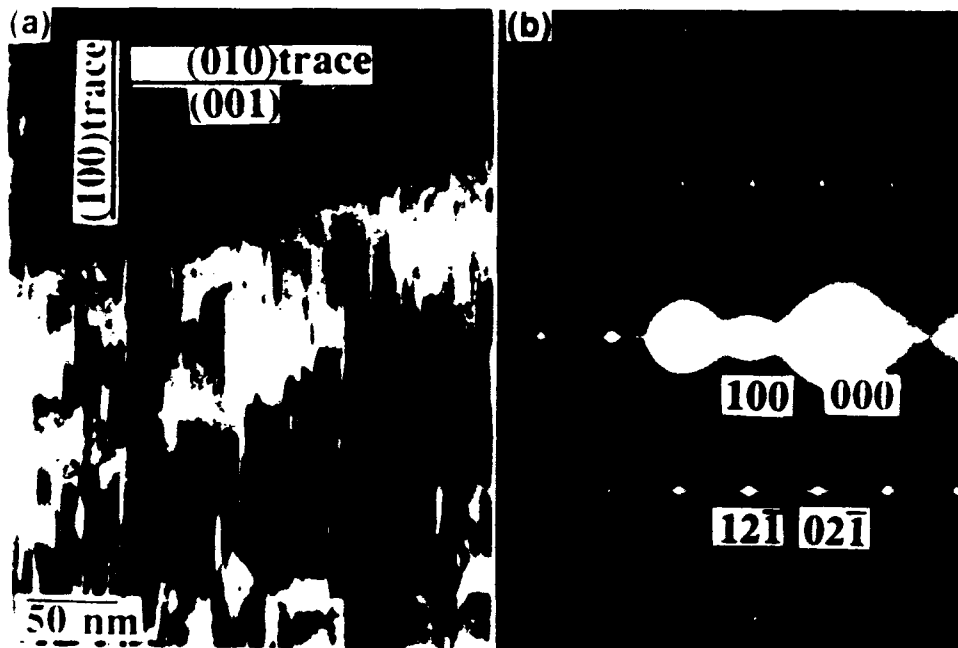
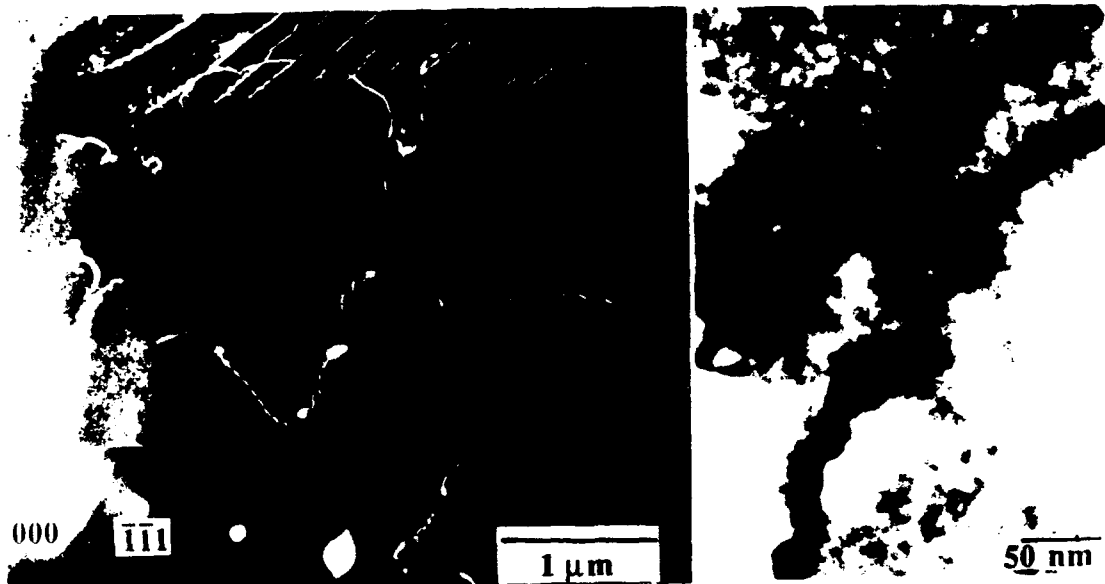


Figure 5. TEM microstructures of AC specimens. (a) Bright-field image with foil plane parallel to (011), (b)  $1\bar{1}1$  dark-field image of (a), (c) bright-field image, and (d)  $11\bar{1}$  dark-field image.



**Figure 6. Fine, plate-like precipitates which have formed on (100) planes. (a) Dark-field image of an ordered (100) reflection, and (b) [012] zone axis of  $L1_2$  phase which shows streaks perpendicular to (100).**



**Figure 7. Weak-beam, dark-field image taken from a  $(\bar{1}\bar{1}\bar{1})$  reflection showing dislocations and fine precipitates in an HHT specimen.**

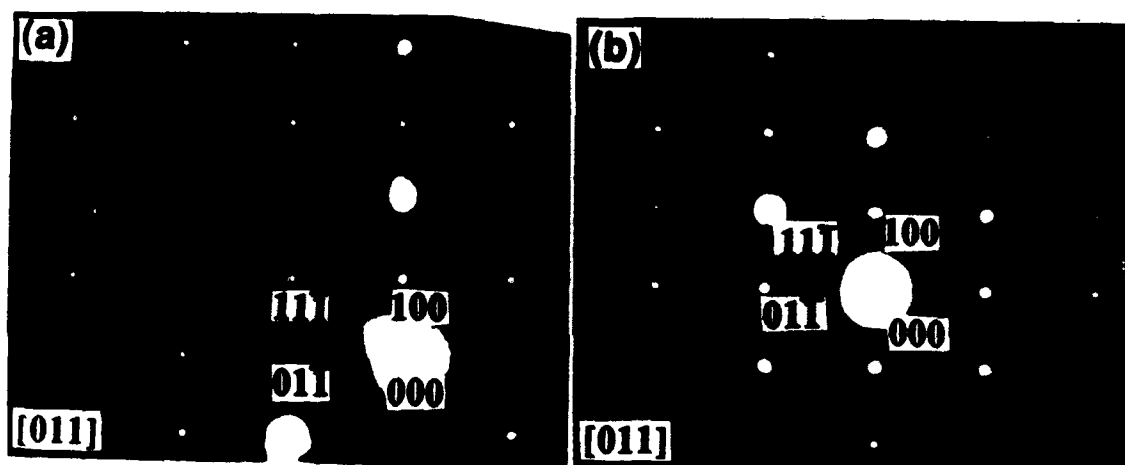


Figure 8. Selected area electron diffraction (SAED) patterns showing the [001] axis in (a) AC and (b) HHT conditions.

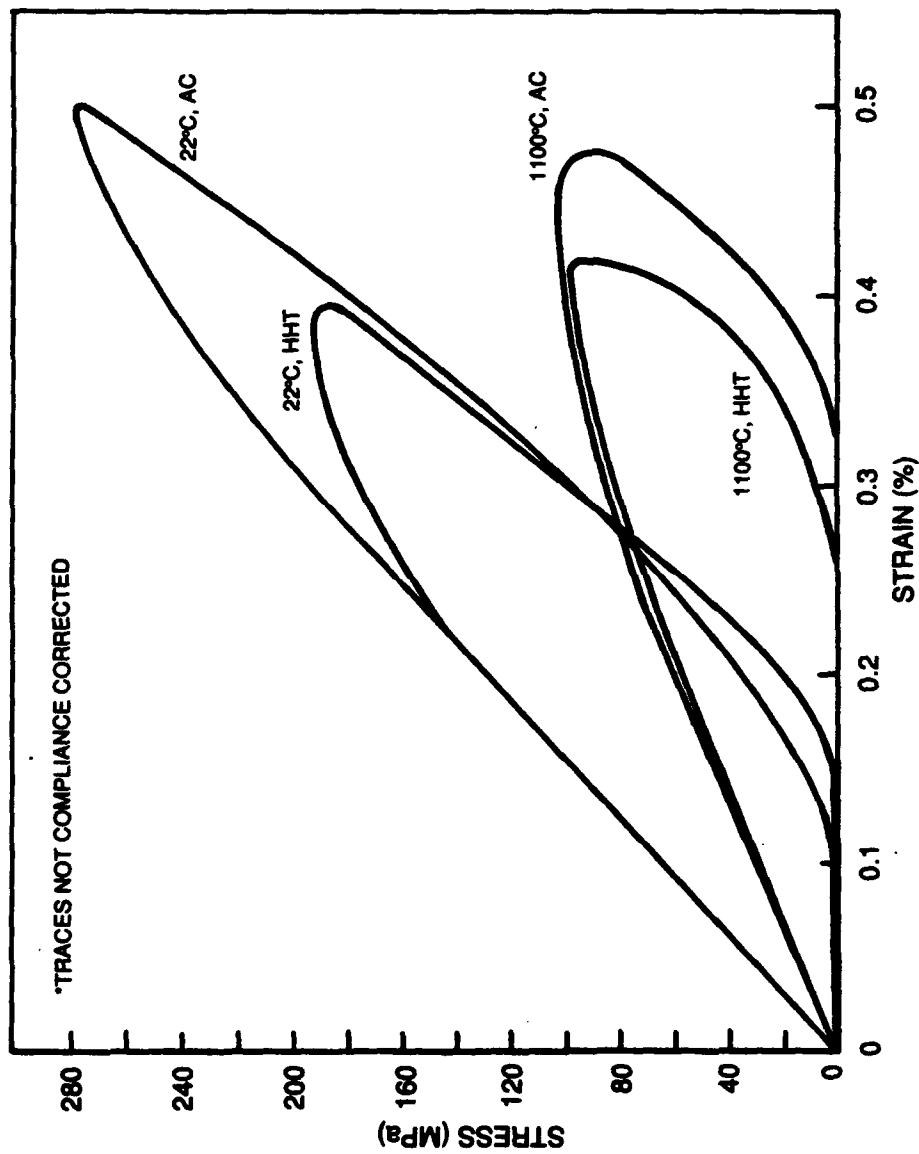


Figure 9. Compressive stress-strain curves for Fe-modified Al-Ti alloy specimens in AC and HHT conditions at 22 and 1100°C.

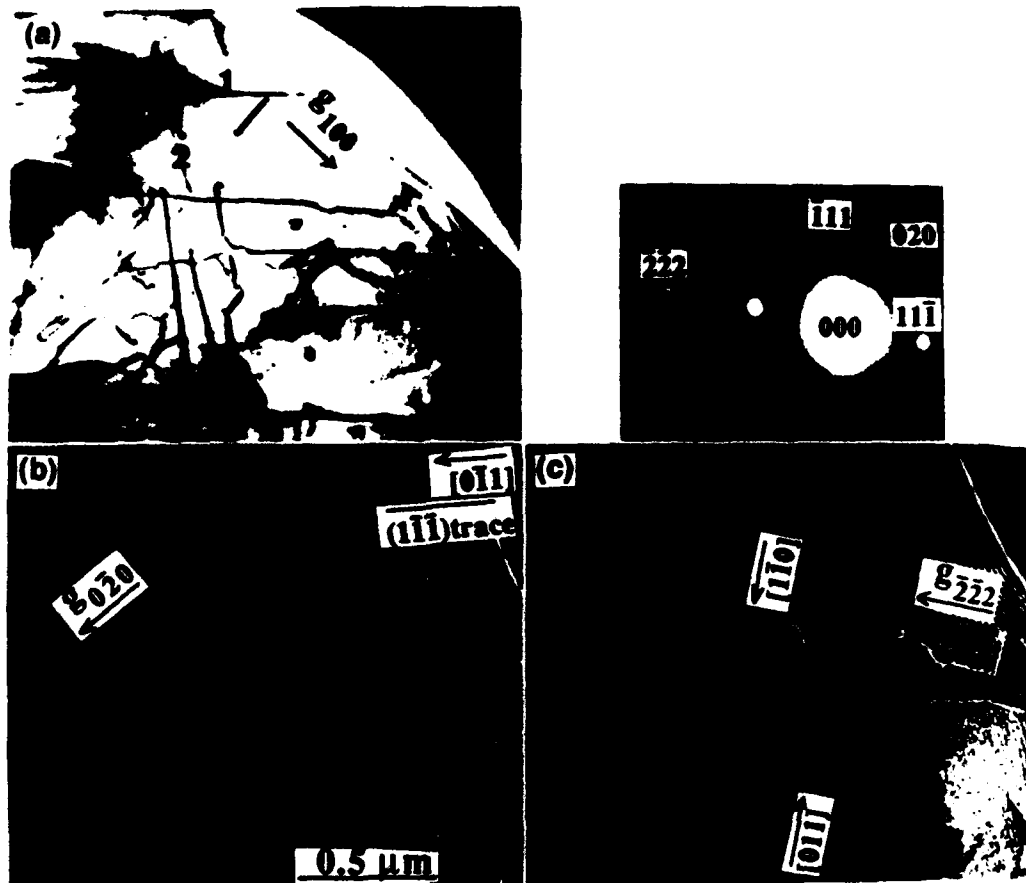


Figure 10. Dislocation structures in a HHT specimen deformed to 0.5% total strain in compression at 1100°C. (a) Bright-field image, (b) weak-beam, dark-field image with a 020 reflection, and (c) weak-beam, dark-field micrograph with a  $(\bar{2}\bar{2}\bar{2})$  reflection and corresponding SAED pattern. Note cross-slipping of dislocations #2 from  $(1\bar{1}\bar{1})$  to  $(100)$  planes.

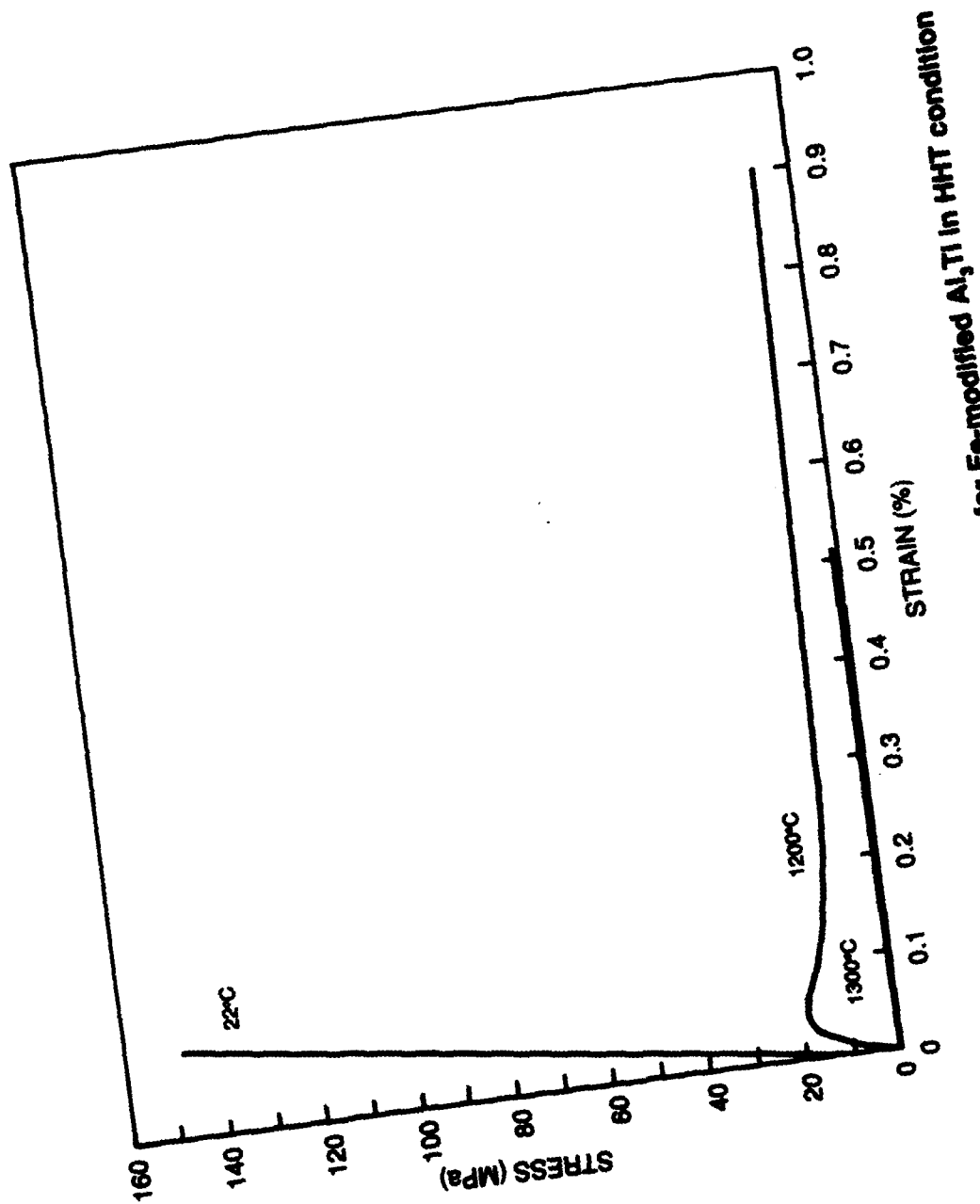


Figure 11. Four-point flexural stress-strain curves for Fe-modified  $\text{Al}_3\text{Ti}$  in HHT condition at 22, 1200, and 1300°C.



**Figure 12.** Transmission electron micrograph of as-arc-cast  $\text{Al}_{67.5}\text{Ti}_{25}\text{Fe}_{7.5}$  alloy, showing a large faulted precipitate.





Figure 13. Dark field micrograph of a homogenized Al<sub>67.5</sub>Ti<sub>28</sub>Fe<sub>7.5</sub> specimen, showing tiny precipitates on dislocations. A (111) L<sub>1</sub><sub>2</sub> reflection has been used.

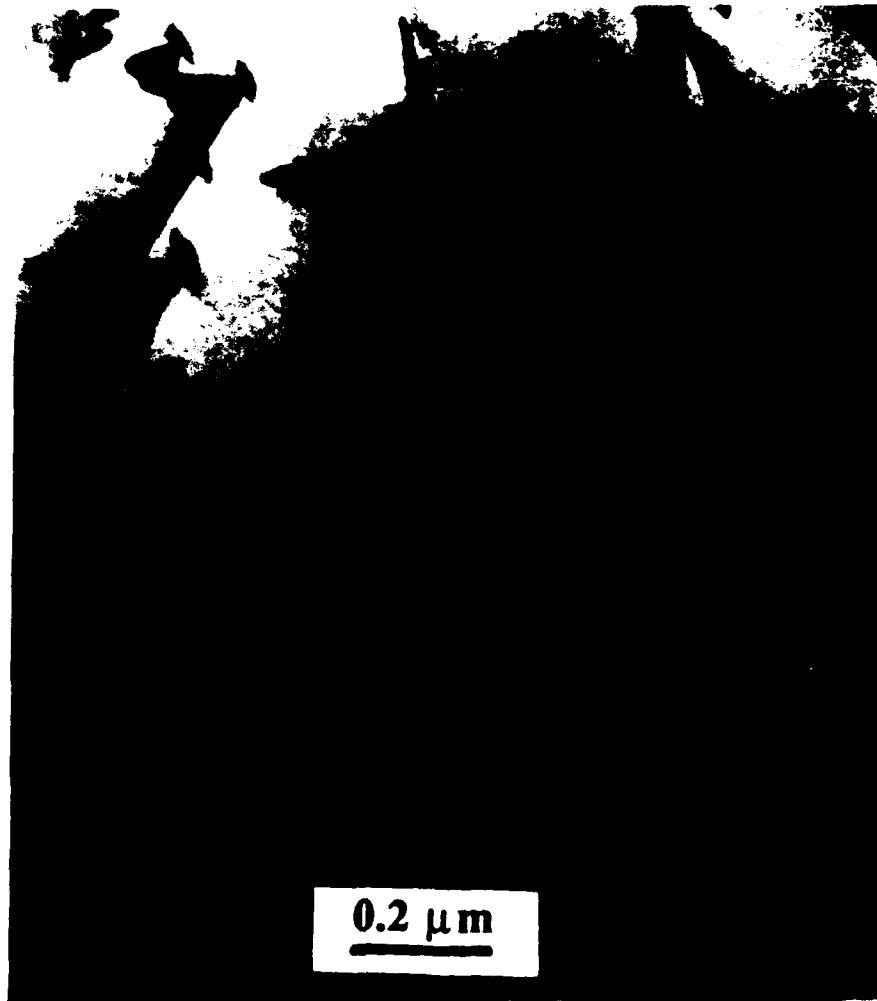


Figure 14. Heterogeneous precipitates along dislocation in an as-arc-cast  $\text{Al}_{67.5}\text{Ti}_{25}\text{Fe}_{7.5}$  specimen.



**Figure 15. Plate-shaped precipitates on three sets of  $\{001\}$  planes of the  $L1_2$  matrix in an as-arc-cast specimen. Foil plane nearly parallel to  $(615)$ .**

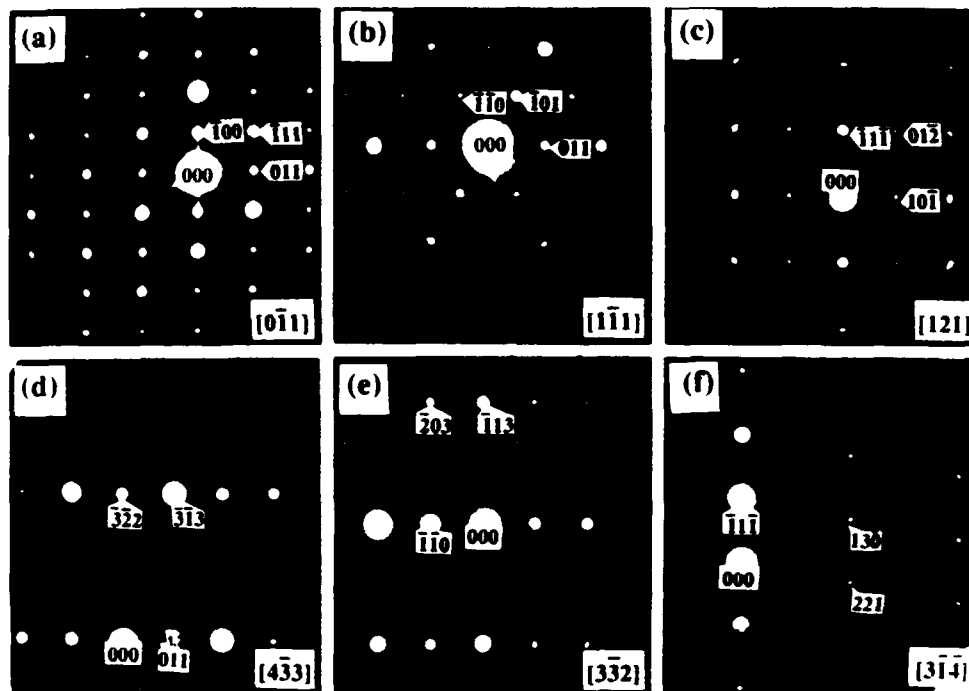


Figure 16. Electron diffraction patterns taken from as-arc-cast  $\text{Al}_{67.5}\text{Ti}_{25}\text{Fe}_{7.5}$  specimens. Zone axes indexed by  $L1_2$ : (a)  $[0\bar{1}1]$ , (b)  $[1\bar{1}1]$ , (c)  $[121]$ , (d)  $[4\bar{3}3]$ , (e)  $[3\bar{3}2]$  and (f)  $[3\bar{1}4]$ .

ZONE AXES AND INDICES OF PRECIPITATES:

- (d) VARIANT 1:  $[8\bar{6}1]$ ; a1: 016; b1:  $\bar{1}08$ ; c1:  $\bar{1}\bar{1}2$ ;  
 VARIANT 2:  $[861]$ ; a2:  $01\bar{6}$ ; b2:  $\bar{1}12$ ; c2:  $\bar{1}08$ ;  
 VARIANT 3:  $[441]$ ; a3:  $1\bar{1}0$ ; b3:  $10\bar{4}$ ; c3:  $01\bar{4}$ ;
- (e) VARIANT 1:  $[9\bar{9}1]$ ; a1: 110; b1: 129; c1: 019;  
 VARIANT 2:  $[641]$ ; a2:  $10\bar{6}$ ; b2:  $01\bar{4}$ ; c2:  $\bar{1}12$ ;  
 VARIANT 3:  $[461]$ ; a3:  $0\bar{1}6$ ; b3:  $1\bar{1}2$ ; c3:  $10\bar{4}$ ;
- (f) VARIANT 1:  $[4\bar{2}\bar{1}]$ ; a1:  $1\bar{1}6$ ; b1: 104; c1: 012;  
 VARIANT 3:  $[8\bar{2}\bar{1}]$ ; a3: 116; b3: 108; c3:  $0\bar{1}2$ .

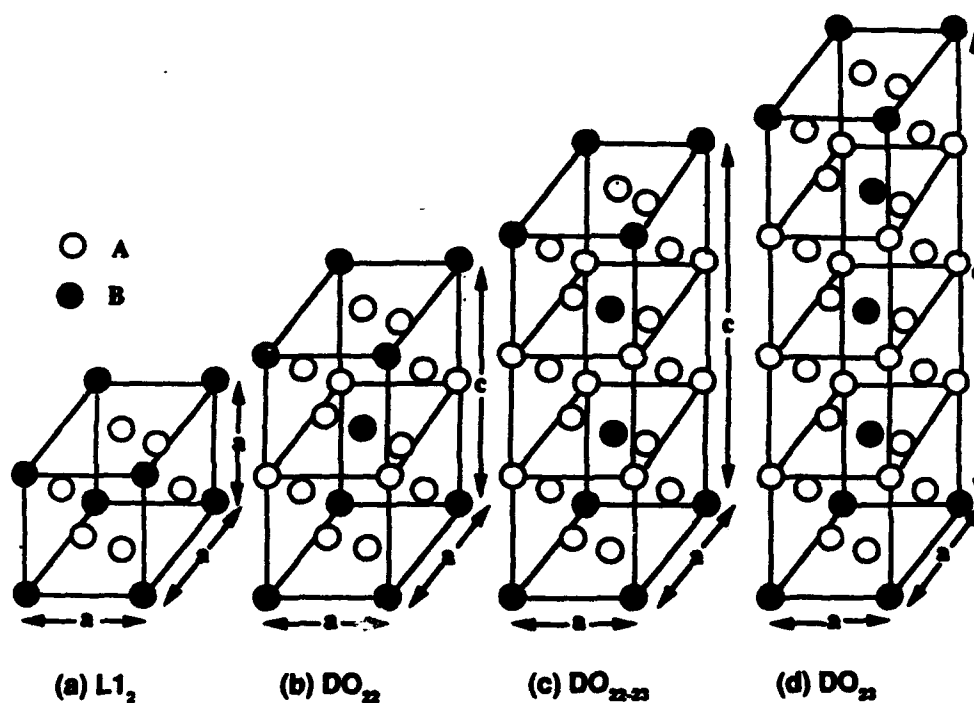
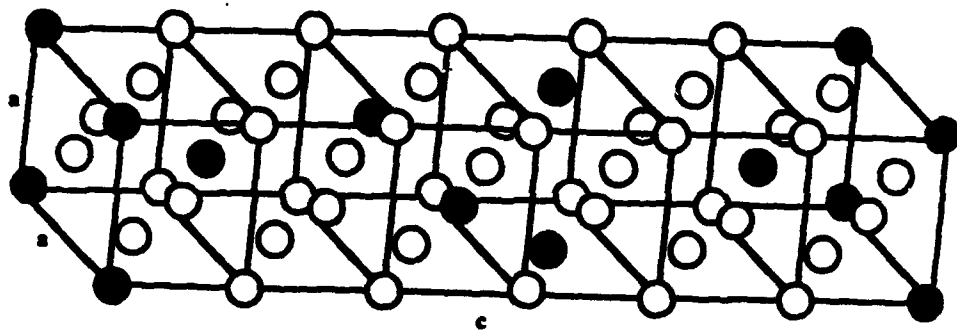


Figure 17. Unit cells of  $L1_2$ -based structures. (a)  $L1_2$ , (b)  $DO_{22}$ , (c)  $DO_{22-22}$ , and (d)  $DO_{22}$ .



**Figure 18. A proposed ordered tetragonal structure consisting of six fcc unit cells.**

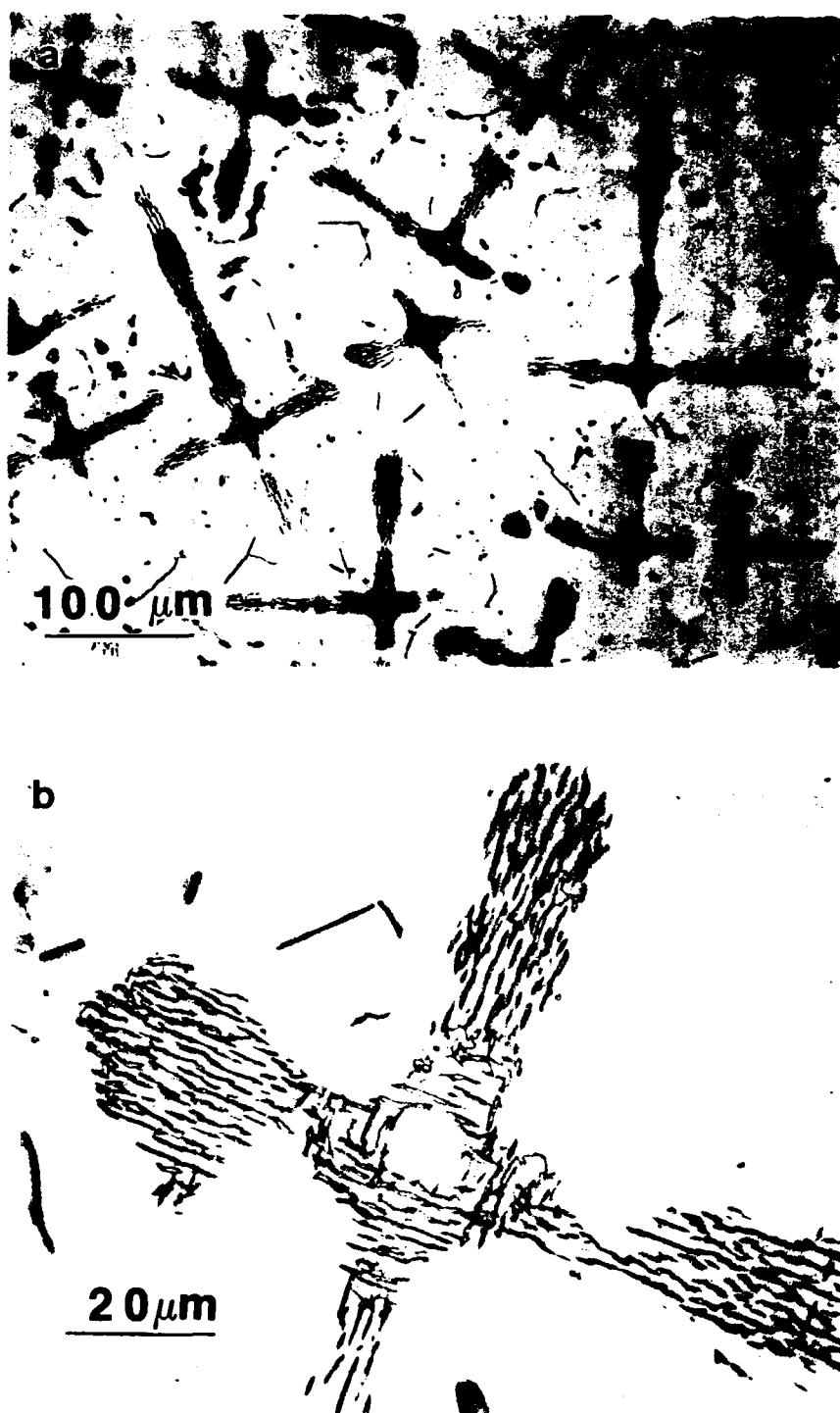


Figure 19. Optical micrographs showing a dendritic structure appearing in HIPed specimens after arc casting (a) low magnification; (b) high magnification.

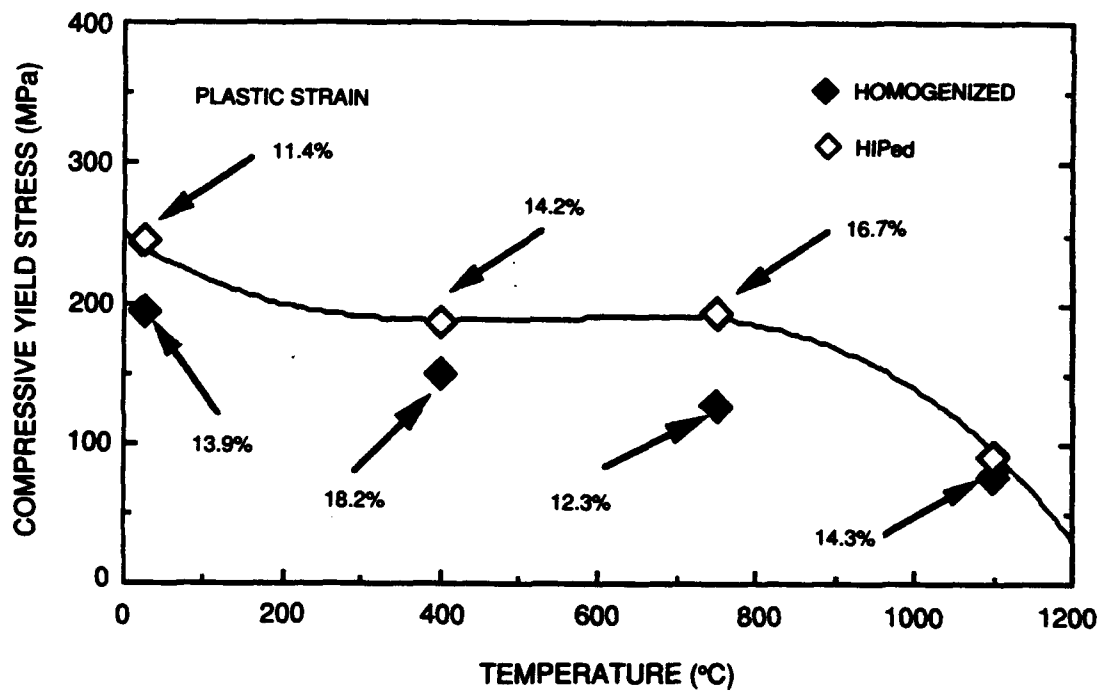
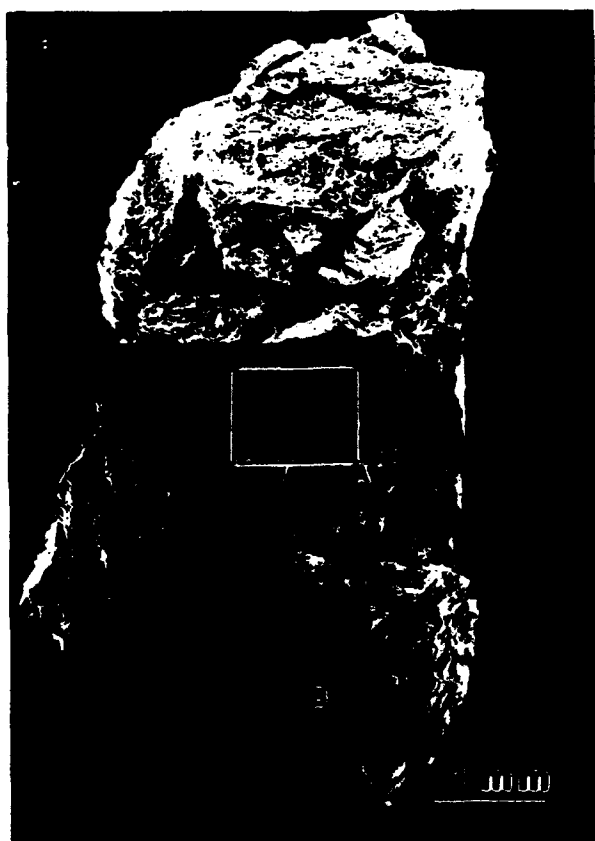
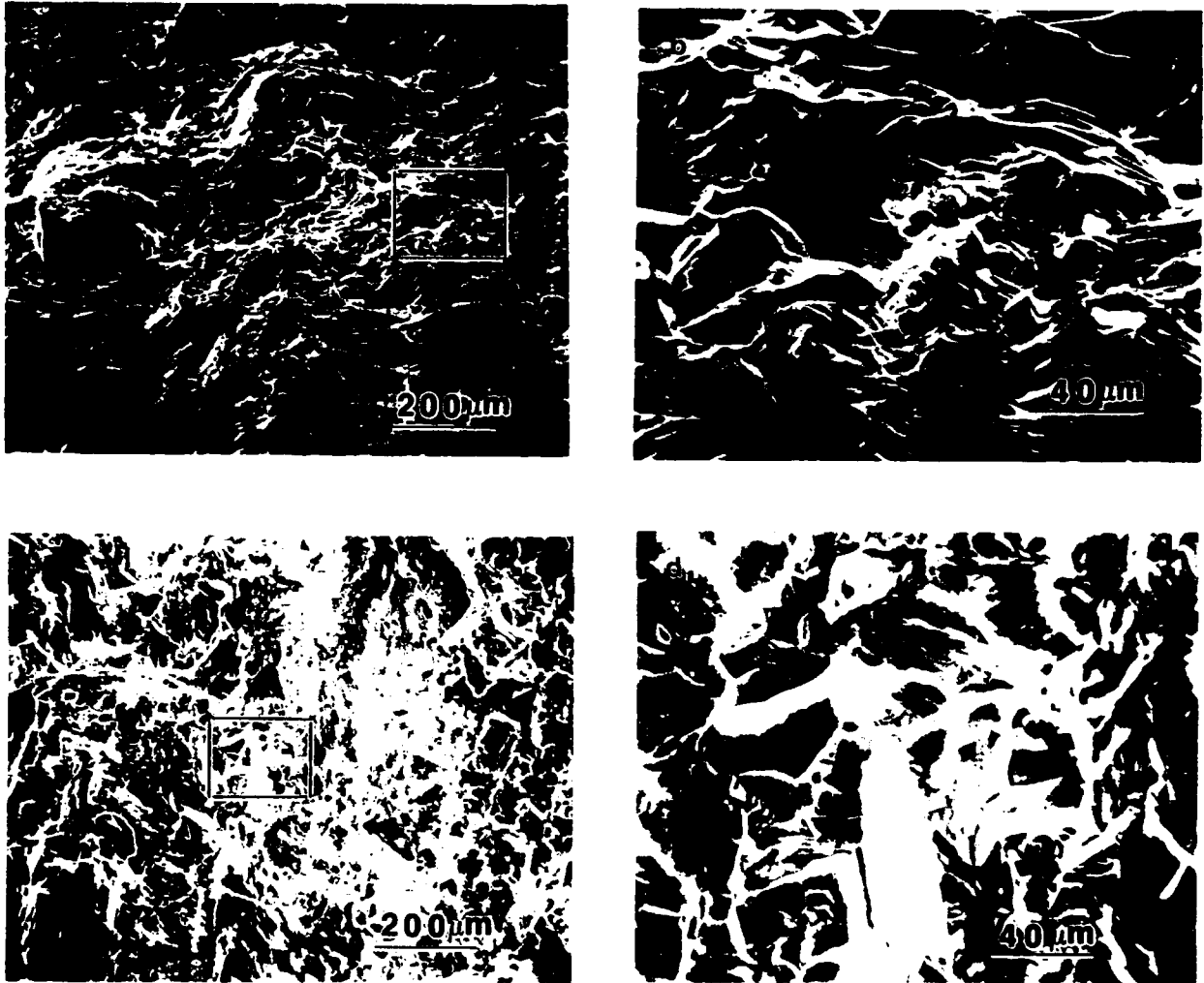


Figure 20. Temperature dependence of yield stress for Fe-modified  $L_{12}$ -type  $Al_3Ti$ .





**Figure 21. Deformed specimens in compression at room temperature. (a) following HHT; (b) following HIP**



**Figure 22** High magnification scanning electron micrographs taken from homogenized and HIPed specimens deformed at room temperature. (a) region A of Figure 21a; (b) framed region of (a); (c) a central region of Figure 21b; and (d) framed region of (c).

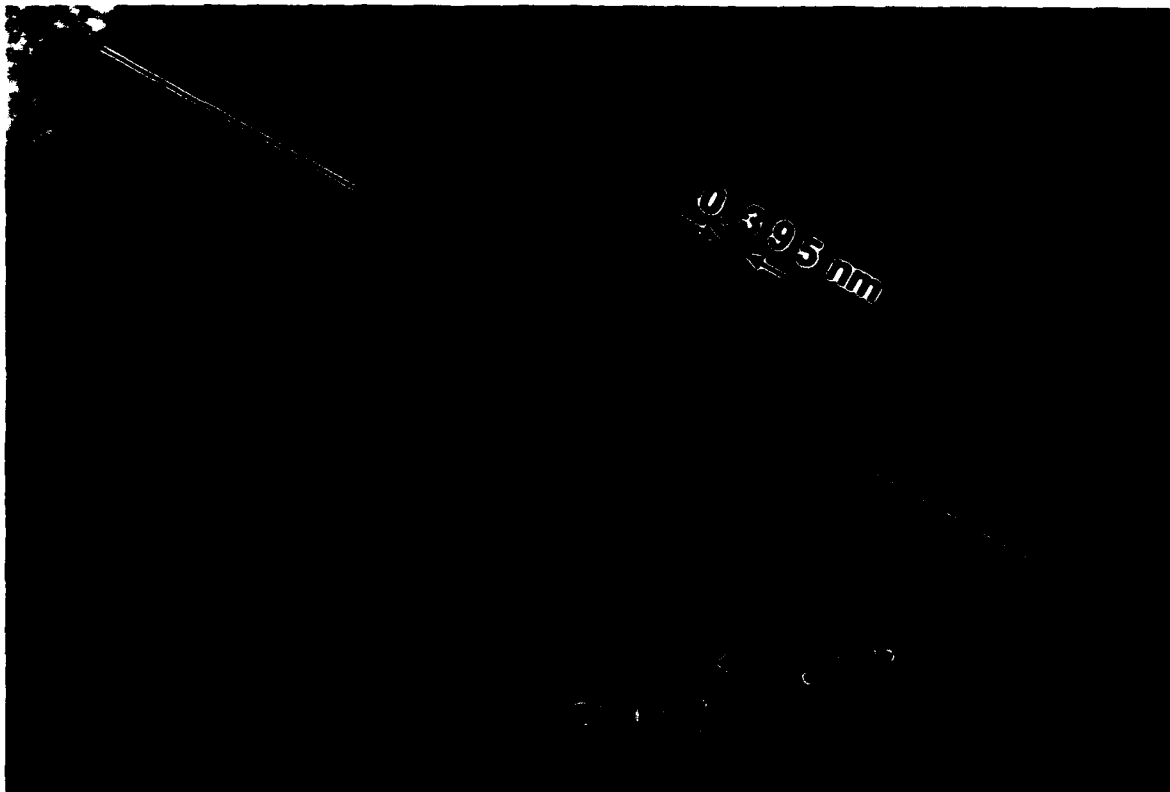


**Figure 23. High-resolution electron micrograph showing pair of superlattice partial dislocations on a (111) plane having Burgers vector  $1/2 [\bar{1}01]$ . Foil plane is (001). Solid lines are on atom plane; dotted lines are between atom planes. Dislocation cores are located near the center between the ends of the lines.**

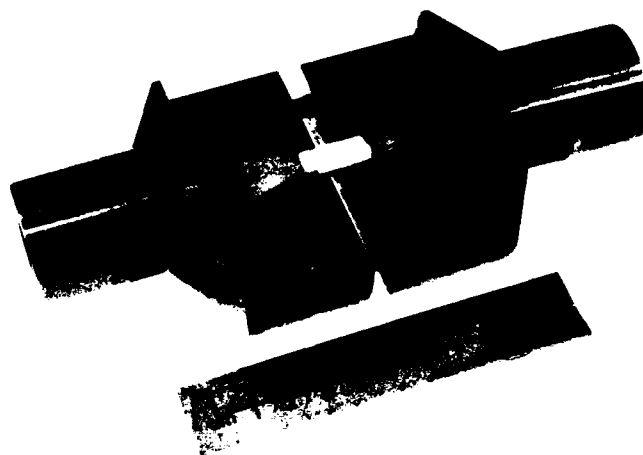
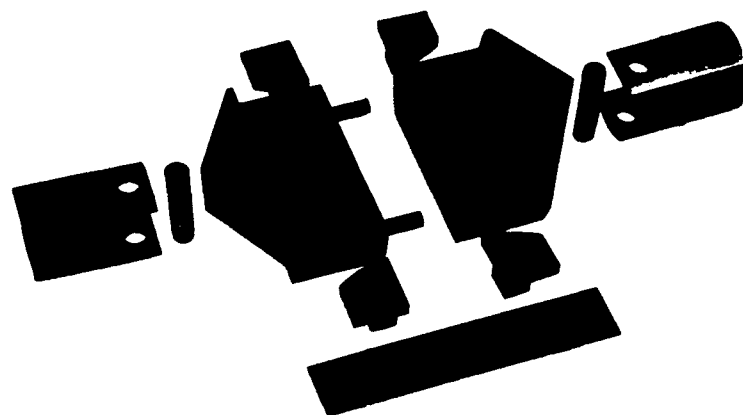
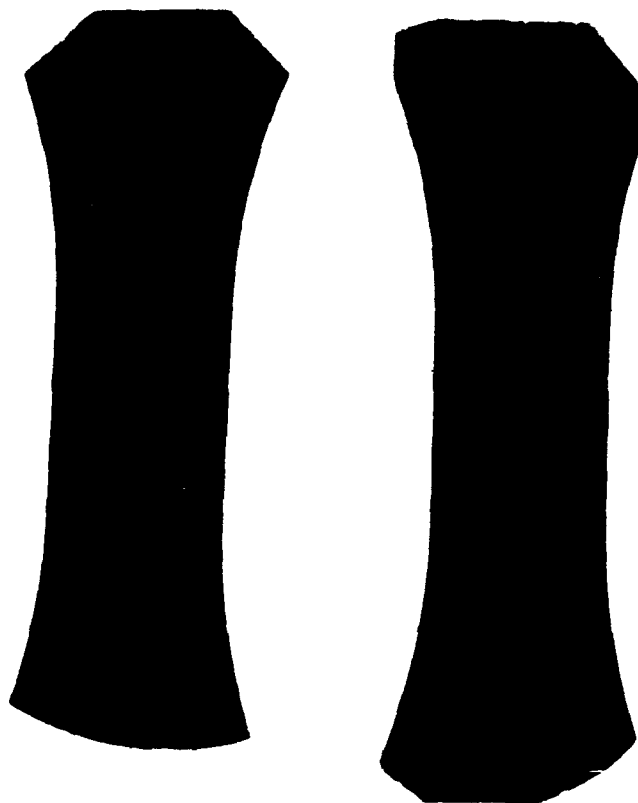
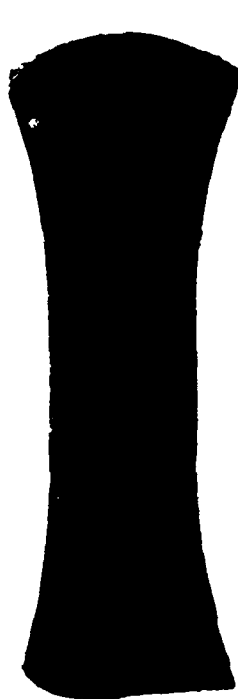


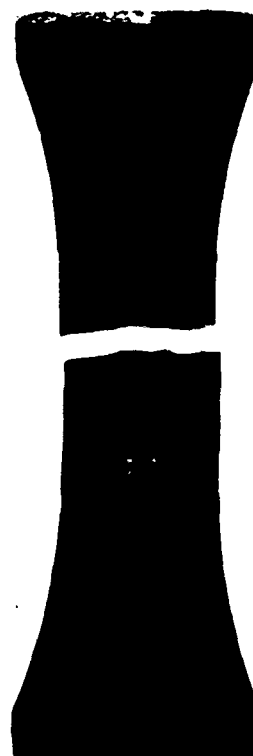
**Figure 24 Assembled and exploded views of tensile/cyclic fixture for brittle materials.**



a) AS EDMed



b) AFTER POLISHING



c) AFTER TESTING

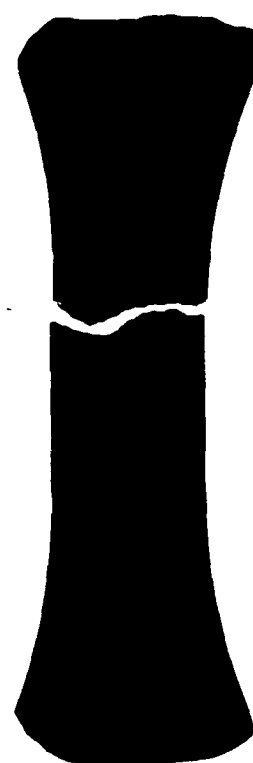
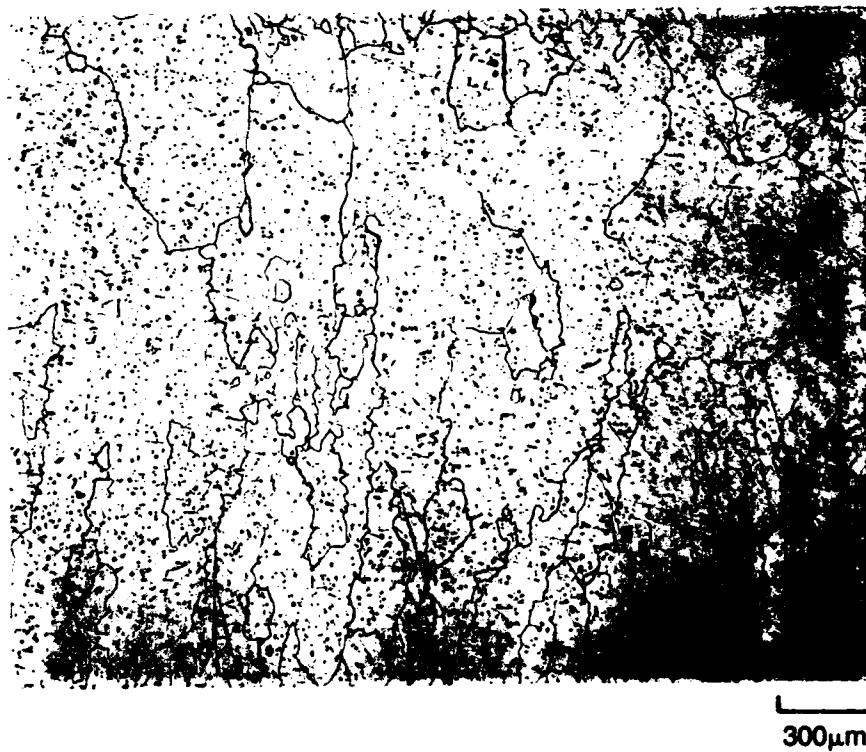


Figure 25. Representative specimens.



**Figure 26** Representative microstructure of Al-25 at% Ti-7.5 at% Fe alloy following casting, HIP at 1050°C, and standard HHT.



**Figure 27** Representative microstructure of Al-25 at% Ti-7.5 at% Fe alloy following casting, HIP at 1100°C, and standard HHT.

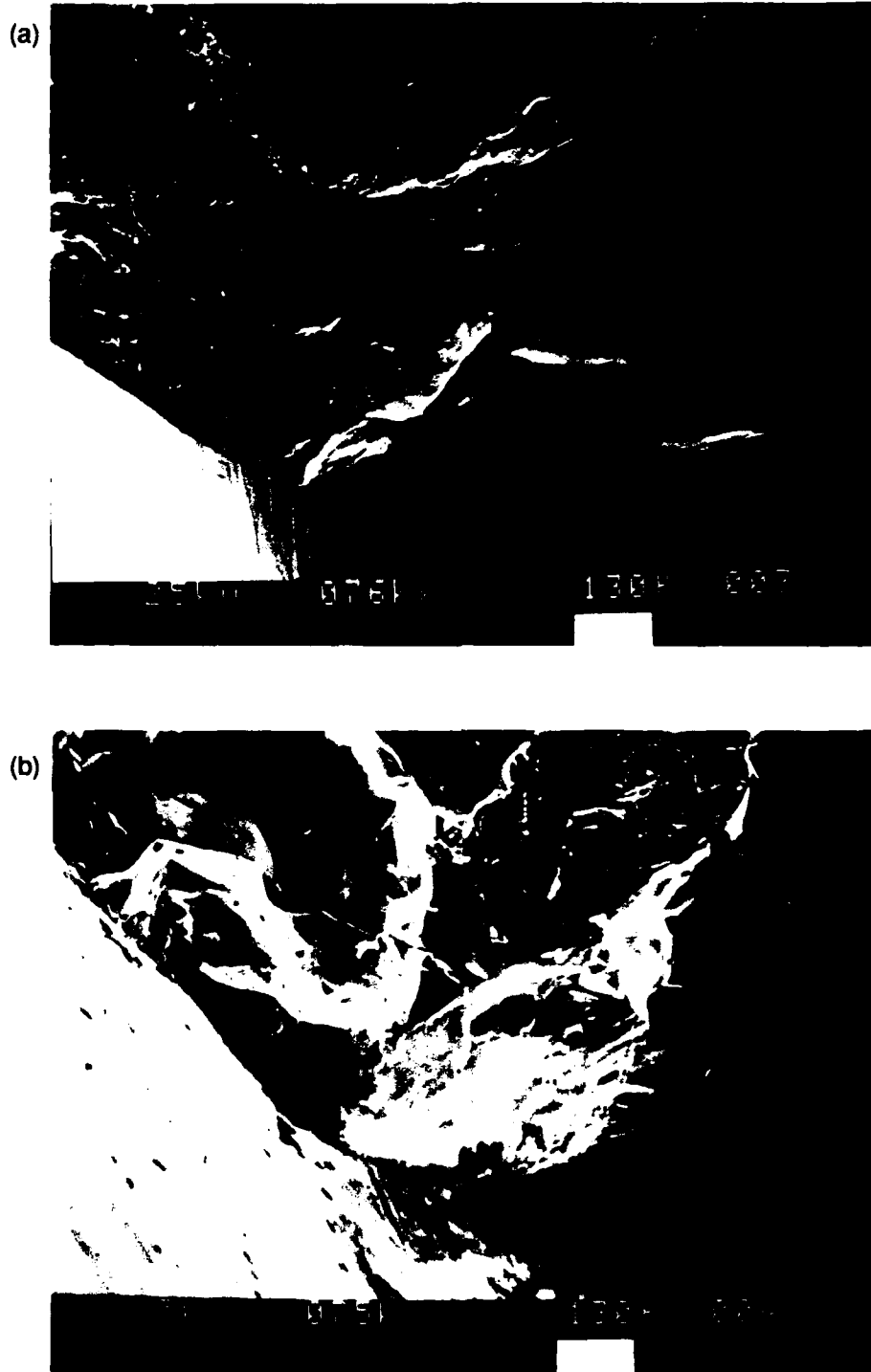
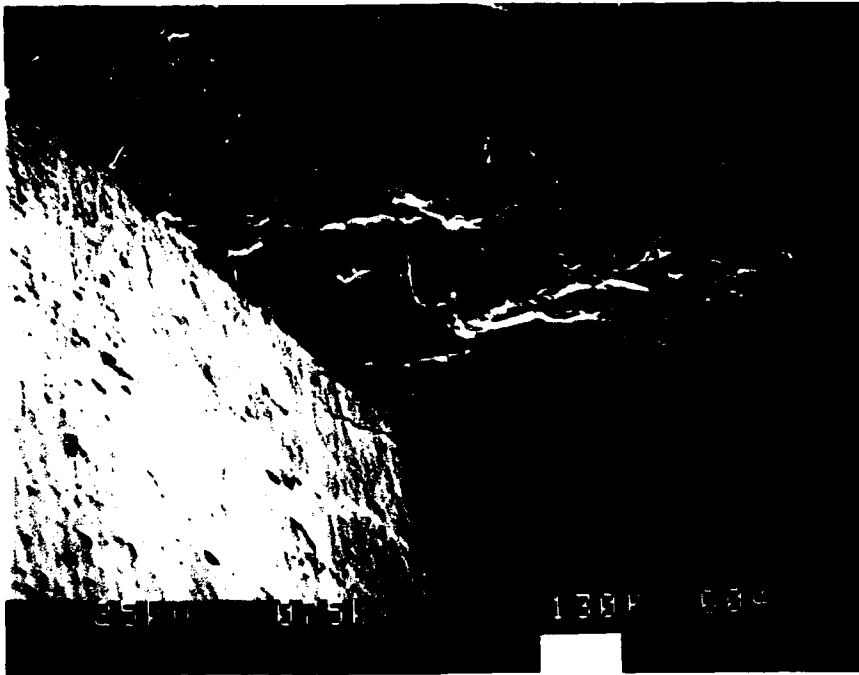


**Figure 28** Fracture surface following monotonic tension at (a) 22°C and (b) 1050°C. HIP temperature for both (a) and (b): 1050°C.

(a)



(b)

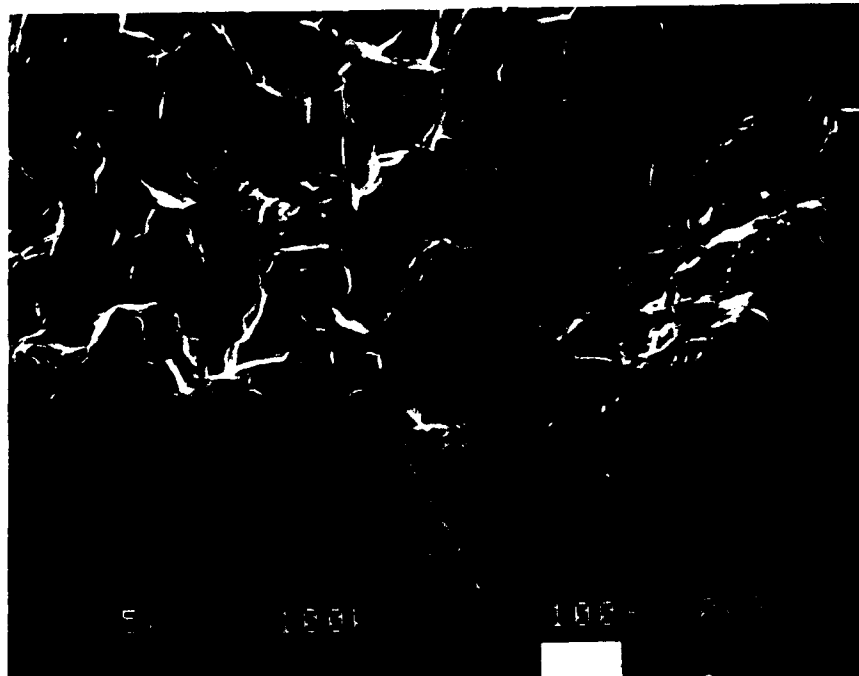


**Figure 29** Fracture surface following monotonic tension at (a) 22°C and (b) 1050°C. HIP temperature for both (a) and (b): 1100°C.



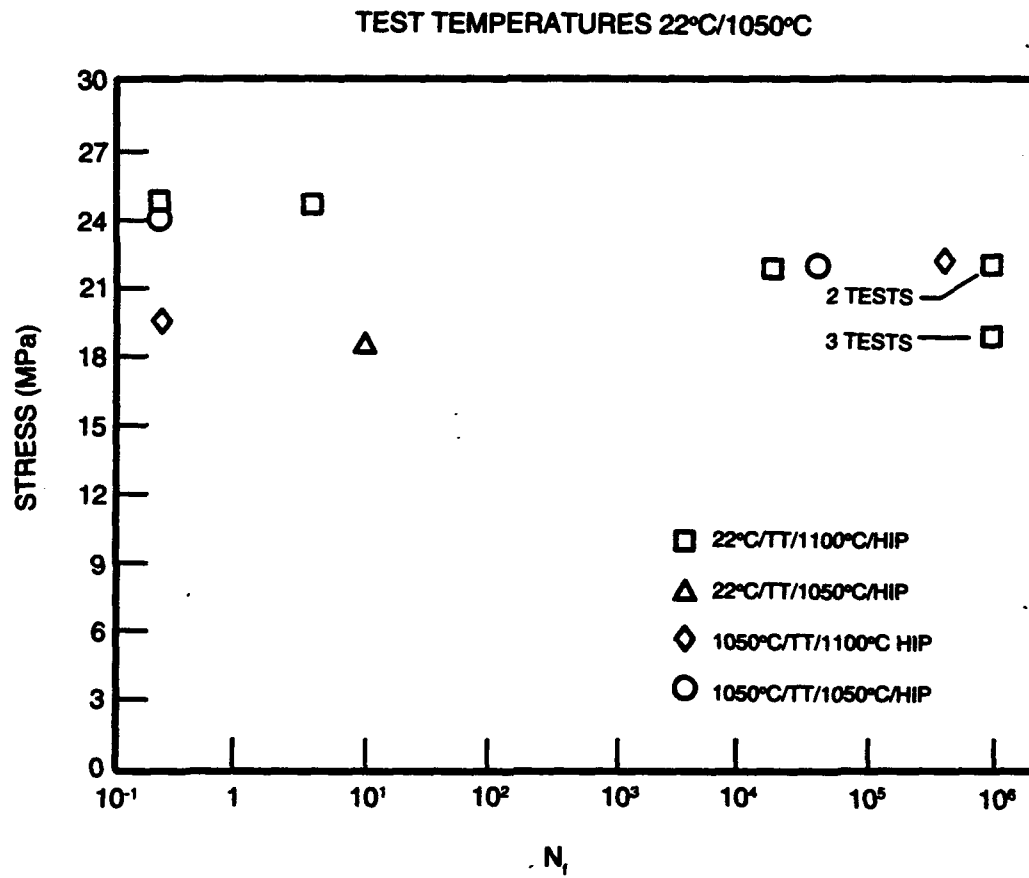


Figure 30 Cyclic tensile properties of Al-25 at% Ti-7.5% Fe alloy following casting, HIP at either 1050 or 1100°C, and standard HHT.



**Figure 31** Surface of specimen which fractured at 22°C following 4 cycles at a maximum stress amplitude of 24.4 MPa. HIP temperature: 1050°C.



**Figure 32** Surface of specimen which fractured at 22°C following 18,000 cycles at a maximum stress amplitude of 21.5 MPa. HIP temperature: 1100°C.

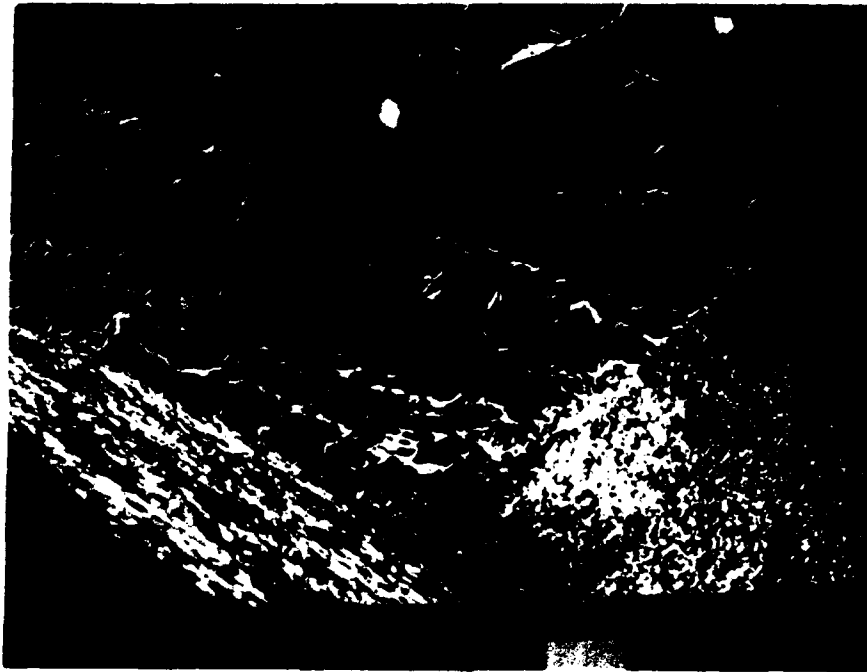


**Figure 33** Fracture surface following 452,000 cycles at a maximum stress amplitude of 21.7 MPa at 1050°C. HIP temperature: 1100°C.

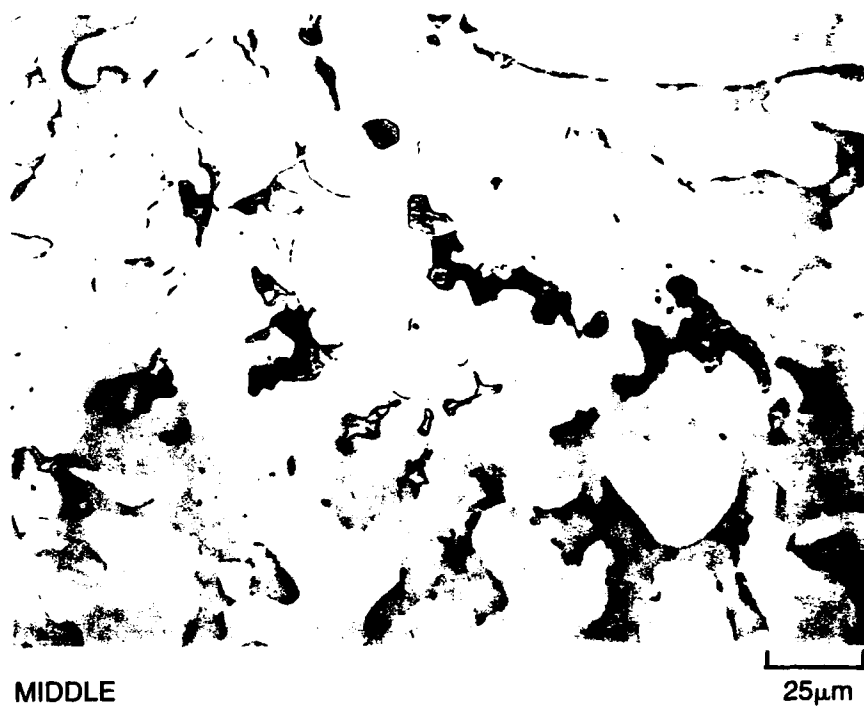


**Figure 34 Representative microstructures of Al-16.75 at% Ti-8.25 at% Nb-7.5 at% Fe following casting and HHT for 240 h.**

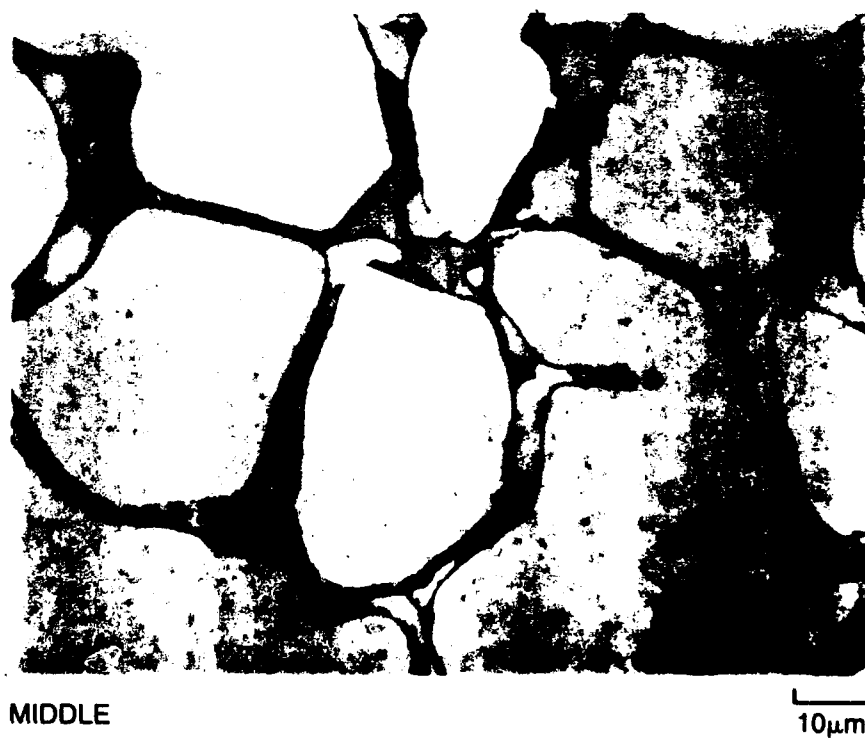
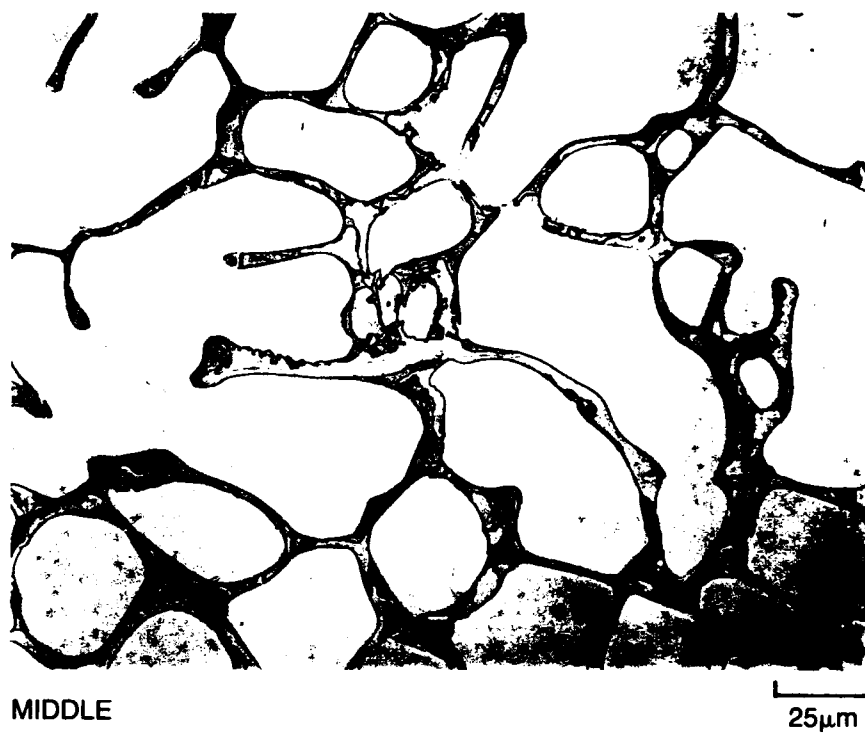


**Figure 35 Representative microstructures of Al-8.25 at% Ti-16.75 at% Nb-7.5 at% Fe following casting and HHT for 240 h.**

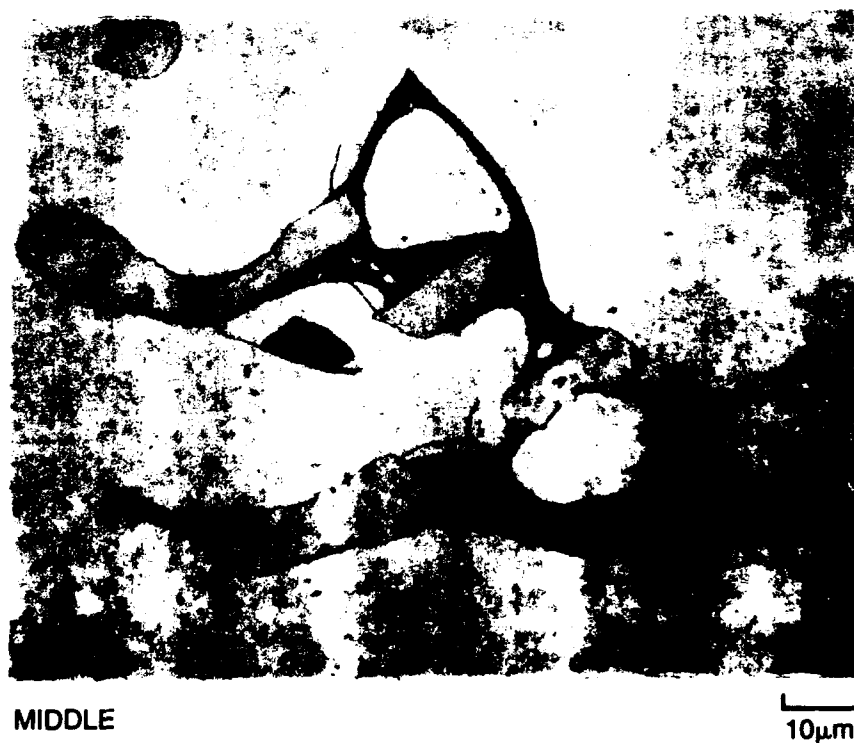


**Figure 36 Representative microstructures of Al-25 at% Nb-7.5 at% Fe following casting and HHT for 240 h.**

**Contract F49620-89-C-0047**

**Professor A. G. Evans  
Dept. of Materials  
Univ. of California  
Santa Barbara, CA 93106**

**Prof. H. R. P Inoue  
Dept. of Mat. Sci. & Eng.  
Univ. of Washington  
302 Roberts Hall, FB-10  
Seattle, WA 98195**

**Dr. Ted Nicholas  
AFWAL/MLLS  
Wright Patterson AFB, OH 45433**

**Dr. Dennis Dimiduk  
AFWAL/MLLM  
Wright Patterson AFB, OH 45433**

**Dr. Daniel Miracle  
WRDC/MLLM  
Wright Patterson AFB, OH 45433**

**Dr. David Davidson  
SouthWest Research Inst.  
P.O. Box 28510  
San Antonio, TX 78228**

**Professor Robert Ritchie  
Univ. of California  
282 Hearst Mining Bldg.  
Berkeley, CA 94720**

**Professor Robert Asaro  
Dept. of Ames R-011  
Univ. of California-San Diego  
La Jolla, CA 92093**